HHS Public Access

Author manuscript

Cell Rep. Author manuscript; available in PMC 2018 December 18.

Published in final edited form as:

Cell Rep. 2018 August 28; 24(9): 2404–2417.e8. doi:10.1016/j.celrep.2018.07.101.

Mitochondrial Complex I Activity Is Required for Maximal Autophagy

Hala Elnakat Thomas[1], **Yu Zhang**[1], **Jonathan A. Stefely**[1,2], **Sonia R. Veiga**[3], **George Thomas**[1,3,4], **Sara C. Kozma**[1,3], and **Carol A. Mercer**[1,5,*]

[1]Division of Hematology/Oncology, University of Cincinnati, Cincinnati, OH, USA

[2]Medical Scientist Training Program, School of Medicine and Public Health, University of Wisconsin-Madison, Madison, WI, USA

[3]Laboratory of Metabolism and Cancer, Catalan Institute of Oncology, ICO, Bellvitge Biomedical Research Institute, IDIBELL, 08908 Barcelona, Spain

[4]Unit de Biochemistry, Department of Physiological Sciences II, Faculty of Medicine, Campus Universitari de Bellvitge-IDIBELL, University of Barcelona, 08908 L'Hospitalet de Llobregat, Barcelona, Catalonia, Spain

[5]Lead Contact

SUMMARY

Cells adapt to nutrient and energy deprivation by inducing autophagy, which is regulated by the mammalian target of rapamycin (mTOR) and AMPactivated protein kinases (AMPKs). We found that cell metabolism significantly influences the ability to induce autophagy, with mitochondrial complex I function being an important factor in the initiation, amplitude, and duration of the response. We show that phenformin or genetic defects in complex I suppressed autophagy induced by mTOR inhibitors, whereas autophagy was enhanced by strategies that increased mitochondrial metabolism. We report that mTOR inhibitors significantly increased select phospholipids and mitochondrial-associated membranes (MAMs) in a complex I-dependent manner. We attribute the complex I autophagy defect to the inability to increase MAMs, limiting phosphatidylserine decarboxylase (PISD) activity and mitochondrial phosphatidylethanolamine (mtPE), which support autophagy. Our data reveal the dynamic and metabolic regulation of autophagy.

In Brief

*Correspondence: mercerc@ucmail.uc.edu.

AUTHOR CONTRIBUTIONS

C.A.M., H.E.T., J.A.S., S.C.K., S.R.V., and G.T. conceived and designed the experiments; C.A.M., Y.Z., H.E.T., and J.A.S. performed the experiments; C.A.M. directed the studies; and C.A.M., H.E.T., Y.Z., J.A.S., S.R.V., S.C.K., and G.T. contributed to the writing of the manuscript.

DECLARATION OF INTERESTS

The authors declare no competing interests.

SUPPLEMENTAL INFORMATION

Supplemental Information includes seven figures and can be found with this article online at https://doi.org/10.1016/j.celrep.2018.07.101.

Autophagy is a survival response to starvation conditions, which inhibit the mTOR kinase. Thomas et al. demonstrate that autophagy induced by mTOR inhibitors is limited by phenformin and defects in OXPHOS but enhanced by strategies that increase mitochondrial energy and phospholipid metabolism. The therapeutic relevance of these findings is discussed.

Graphical Abstract

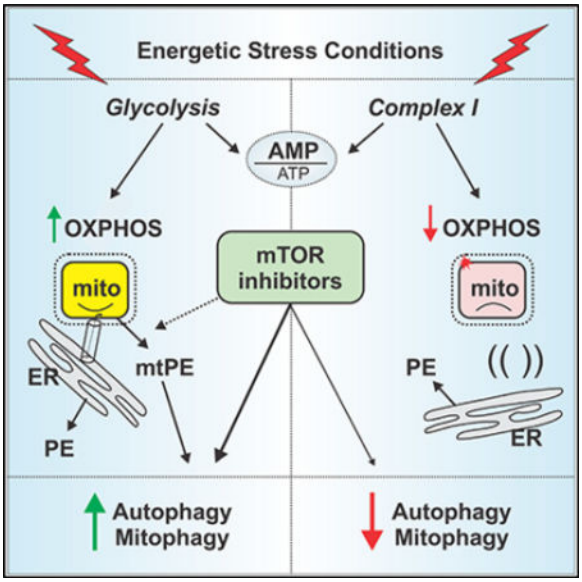

INTRODUCTION

Autophagy targets long-lived proteins, complex molecular structures, and organelles for lysosomal degradation, maintaining homeostasis under basal conditions and generating molecular building blocks to support essential cellular processes during starvation. The term autophagy in the broadest sense includes macroautophagy, microautophagy, and chaperone-mediated autophagy (Yang and Klionsky, 2010). The multistep process of macroautophagy, which we will call autophagy, responds to signals that trigger (1) the formation of double-membrane autophagosomes to sequester cargo, (2) trafficking along microtubules, (3) fusion with the lytic compartment, and (4) enzymatic degradation of contents to be released and recycled. Autophagy is thus a catabolic process to supply metabolites for anabolic processes. However, autophagy is anabolic in that it requires the continued biosynthesis of autophagosomes, involving the coordinate regulation of autophagy proteins, lipids, and sufficient energy at localized regions of assembly (Kaur and Debnath, 2015; Yang and Klionsky, 2010). It is now recognized that autophagy, initially thought to be nonselective in the sequestration of cargo, is often selective, using adaptors or receptors to link specific cargo such as mitochondria to the growing autophagosome (Farré and Subramani, 2016).

Autophagy is regulated by three interrelated protein kinases: the mammalian target of rapamycin (mTOR), Unc-51-like kinase 1 (ULK1), and AMP-activated protein kinase (AMPK) (reviewed by Russell et al., 2014). mTOR's role in autophagy was established more than 20 years ago and is conserved from yeast to mammals. Specifically, TOR in yeast

inhibits the activity of the autophagy-related 1 kinase (Atg1), similar to mTOR's inhibition of ULK1, albeit with mechanistic differences (reviewed in Noda, 2017). Autophagy is induced by starvation and rapamycin, inhibitors of mTOR complex (mTORC) 1 (Yang and Klionsky, 2010), and by next-generation mTOR kinase inhibitors, which are more potent inhibitors of mTORC1 and mTORC2 (Thomas et al., 2012). However, it is possible to inhibit mTORC1 without activating autophagy; for example, both mTORC1 and autophagy are inhibited by lysosome inhibitors (Amaravadi et al., 2011; Zoncu et al., 2011).

An understanding of AMPK's role in autophagy was complicated by early reports that the AMPK activator 5-aminoimidazole-4-carboxamide ribonucleotide (AICAR) inhibited autophagy (Samari and Seglen, 1998), which was later found to be independent of its effects on AMPK (Meley et al., 2006). Reports that energy deprivation and subsequent activation of AMPK were sufficient, if not required, to inhibit mTOR (Gwinn et al., 2008; Inoki et al., 2003; Kalender et al., 2010) suggested that AMPK induced autophagy through inhibition of mTOR. A more direct role was established when AMPK was shown to phosphorylate ULK1 (Egan et al., 2011; Kim et al., 2011). The latter studies used multiple tools, including AICAR, to activate AMPK and define ULK1 phosphorylation sites, although AICAR, as mentioned earlier, does not induce autophagy (Samari and Seglen, 1998).

There are conflicting reports about the ability of other AMPK activators to induce autophagy, e.g., glucose starvation or phenformin (Ramirez-Peinado et al., 2013; Cheong et al., 2011). These discrepancies may be caused by differences in cell types, assay conditions, or methods to measure autophagy or may reflect that the steps of autophagy require energy (Plomp et al., 1989; Schellens and Meijer, 1991). Phenformin, described as an inhibitor of mitochondrial complex I (Owen et al., 2000), and glucose starvation have different effects on energy metabolism by targeting oxidative phosphorylation (OXPHOS) and glycolysis, respectively. It has been argued that autophagy in response to glucose starvation maintains energy homeostasis by supplying substrates for the tricarboxylic acid (TCA) cycle (Cheong et al., 2011), similar to reports that RAS oncogene-driven tumors are addicted to autophagy to support metabolism and growth (Guo et al., 2016; Yang et al., 2011). However, in cells treated with phenformin, the role of autophagy in the switch to and support of aerobic glycolysis is not clear. The use of phenformin is complicated by reports that it, like AICAR, does not induce autophagy (Cheong et al., 2011). Others suggest that by targeting OXPHOS, phenformin induces selective mitophagy (Shackelford et al., 2013) to maintain energy equilibrium through a mechanism that involves phosphatase and tensin homolog (PTEN)-induced putative kinase 1 (PINK1) and the E3 ubiquitin-protein ligase PARKIN (Youle and Narendra, 2011). In yeast, however, defects in mitochondrial respiration suppress rather than induce autophagy (Graef and Nunnari, 2011). These inconsistencies raise questions about the level of autophagy or mitophagy induced by phenformin or the related biguanide, metformin, a commonly used anti-diabetic drug. Phenformin and metformin are under clinical investigation for pathologies in which autophagy's role is significant, including cancer and neurodegenerative disease (Lorin et al., 2013; Menzies et al., 2017). Therefore, it is critical to understand the degree to which agents that activate AMPK affect autophagy to optimize treatments for the desired outcome.

We initially set out to compare AMPK activators with mTOR inhibitors for their potency to induce autophagy and mitophagy. We found that phenformin and glucose starvation had opposing effects on autophagy and mitophagy, leading to a major shift in our understanding of how energetic stress affects autophagy. Autophagy was suppressed by phenformin and defects in complex I but enhanced by glucose starvation and strategies to increase mitochondrial metabolism. Furthermore, we demonstrate that complex I activity was required for changes in phospholipid metabolism and mitochondrial-associated membrane (MAM) formation, which were increased by mTOR inhibition and important for autophagy. Our findings demonstrate the importance of metabolism in the regulation of autophagy, increase our understanding of the biological effects of clinically relevant biguanides, and suggest strategies to activate or suppress this vital process.

RESULTS

Phenformin Inhibits Autophagy

As a positive control for autophagy, we combined the allosteric and kinase mTOR inhibitors RAD001 and BEZ235 (RB), which we had used previously in a preclinical model of hepatocellular carcinoma (HCC) (Thomas et al., 2012). As an energetic stressor, we initially chose phenformin, because it enters cells more readily than metformin and is reported to be 10 times more potent (Shackelford et al., 2013). These studies were performed primarily in HEK293 cells, which are capable of mounting a robust autophagy response to starvation conditions or mTOR inhibitors (Mercer et al., 2008, 2009; Thomas et al., 2012) and are used routinely for studies associated with mTOR and AMPK signaling (Auciello et al., 2014; Sancak et al., 2010). Consistent with our previous work (Thomas et al., 2012), RB strongly induced autophagy, as determined by the betaine homocysteine S-methyltransferase (BHMT) autophagy cargo assay and accumulation of a glutathione S-transferase (GST)-BHMT fragment; by increased levels of LC3-II, a marker of autophagy (Kabeya et al., 2000); and by decreased levels of sequestome 1 (SQSTM1/p62), an adaptor protein that selects ubiquitinated proteins for autophagy (Pankiv et al., 2007) (Figures 1A and 1B). Unexpectedly, in phenformin-treated cells, BHMT fragmentation and LC3-II levels did not increase and SQSTM1/p62 levels were stable, despite activation of AMPK and inhibition of mTORC1 at later time points, as determined by increased phosphorylation of acetyl-coA carboxylase (ACC) and decreased phosphorylation of S6K1 and 4EBP1 (Figures 1A and 1B). We subsequently tested increasing doses of phenformin for their ability to inhibit mTOR and induce autophagy and found that phenformin did not induce autophagy at any dose and suppressed the amplitude of autophagy induced by RB in a dose-dependent manner (Figure 1C). These results were supported by LC3-II flux analyses by western blotting (Figures 1D and 1E) and immunofluorescence of LC3B puncta (Figures 1F and 1G). These findings were not cell line or compound specific, because the biguanides inhibited autophagy induced by mTOR inhibitors in multiple cell lines, including liver kinase B1 (LKB1)-deficient A549 cells (Figures S1A–S1C), suggesting that AMPK activation is not required for either the induction of autophagy by RB or its inhibition by phenformin. Expression of proteins associated with ULK1 or class III phosphatidylinositol (PtdIns) lipid kinase, VPS34, which define complexes that initiate autophagy were not changed by either treatment (Figure S1D). Finally, rotenone and oligomycin, inhibitors of complex I and ATP

synthase, respectively, did not induce autophagy and inhibited RB-induced autophagy at two time points (Figure S1E), suggesting that respiration-competent mitochondria are essential for autophagy. We conclude that phenformin does not induce autophagy, despite mTOR inhibition and AMPK activation, and inhibits autophagy induced by mTOR inhibitors.

Phenformin Inhibits Mitophagy

We reported that phenformin caused mitochondrial fragmentation and dysfunction in Huh7 cells (Veiga et al., 2018), conditions that are conducive for mitophagy (Pickles et al., 2018) and consistent with reports that phenformin induces mitophagy (Egan et al., 2011; Shackelford et al., 2013). Mitochondria in phenformin-treated HEK293 cells also appeared fragmented and shifted from dense to more buoyant fractions on a density gradient (Figures S2A and S2B). To measure mitophagy, we used the GST_{LSCS}GFP-ActA mitophagy assay, which detects the autolysosomal degradation of a reporter protein embedded in the outer mitochondrial membrane (OMM) (Dennis and Mercer, 2009).

Mitophagy was induced in cells treated with mTOR inhibitors (RB), as determined by increased fragmentation of GST_{LSCS}GFP-ActA, increased LC3-II (Figure 2A), and a significant reduction in mitochondrial mass (Figure 2B). These data are consistent with our previous findings that RB induced mitophagy in mouse liver tumors (Thomas et al., 2012) and the decreased mitochondrial mass reported in cells treated with other mTOR kinase inhibitors (Morita et al., 2013). To determine whether the decreased mitochondrial mass could be attributed to decreased mitochondrial biogenesis, we measured expression of peroxisome proliferator-activated receptor gamma coactivator 1 alpha (PGC1α), nuclear-respiratory factor 1 (NRF1), and transcription factor A, mitochondrial (TFAM), which are reported to be regulated by mTORC1 (Cunningham et al., 2007; Morita et al., 2013). However, in the conditions used here, these transcriptional regulators were not decreased by RB but instead were either unchanged or increased (Figures S2C–S2E). Phenformin did not induce mitophagy when used alone and inhibited RB-induced mitophagy (Figure 2A), similar to its inhibition of autophagy. To confirm these data, we employed mitophagy reporter proteins fused to Keima as described (An and Harper, 2018). Keima is an acid-stable fluorescent protein that emits green or red signals at neutral or acidic pH, respectively, and has been used to determine autophagy flux (An and Harper, 2018; Katayama et al., 2011). In cells expressing Mito-Keima, RB induced readily identifiable discreet red puncta suggestive of active mitophagy, whereas there was little difference in the red signal among vehicle (V), P, or RB plus P (RBP) treatments (Figure 2C). The mitochondrial import receptor subunit TOMM20-Keima fusion protein on the OMM is processed by lysosomal proteases to produce an acid-stable form of ~25 kDa. (An and Harper, 2018). Similar to the GST_{LSCS}GFP-ActA assay (Figure 2A), the processed TOMM20-Keima fragment was increased by RB, but not phenformin (Figure S2F). In TOMM20-Keima cells that overexpressed PARKIN, Keima processing was blunted (Figure S2F), which may be because of PARKIN's E3 ubiquitin ligase activity and increased proteasome degradation of OMM proteins (Yoshii et al., 2011). Further investigation showed that expression of PINK1, which is stabilized on the OMM of damaged mitochondria (Narendra et al., 2010), did not change in cells treated with RB, phenformin, metformin, or rotenone, in contrast to its robust expression in cells treated with oligomycin and antimycin A, inhibitors of mitochondrial

ATP synthase and complex III, respectively, or carbonyl cyanide 3-chlorophenyl hydrazone (CCCP), a mitochondrial uncoupler (Figure S2G). The increased mitophagy observed with RB correlated with decreased levels of TOM20 on the OMM (Figure S2G), but not with cytochrome c oxidase assembly protein COX II on the inner mitochondrial membrane (IMM) (Figure 2A). Furthermore, mitochondrial complex I activity was increased in mitochondria from RB-treated cells but was not significantly changed by phenformin (Figure 2D). The assay employed for these measurements does not depend on ubiquinone, so complex I inhibitors that interfere with the ubiquinone binding site, such as rotenone (Palmer et al., 1968), do not inhibit activity. Phenformin may work through a similar mechanism. We conclude that RB-induced mitophagy is distinct from a PINK1/PARKIN mechanism of mitophagy and is a type of mitochondrial remodeling that preserves complex I activity. We found no evidence of mitophagy in phenformin-treated cells, which may be partly because of the lack of PINK1 stabilization. Despite this, phenformin inhibited mitophagy induced by RB, suggesting that a common mechanism underlies phenformin's inhibition of both autophagy and mitophagy.

Phenformin's Inhibition of Autophagy Is Not Explained by Lysosome Defects

The inhibition of autophagy by phenformin could be attributed to several mechanisms, including inhibition of mitochondrial complex I, mitochondrial glycerophosphate dehydrogenase, one-carbon metabolism, or the lysosome (Corominas-Faja et al., 2012; Lockwood, 2010; Madiraju et al., 2014; Owen et al., 2000). The latter was of particular interest, because lysosome dysfunction inhibits both mTORC1 and autophagy (Amaravadi et al., 2011; Zoncu et al., 2011) and metformin and phenformin inhibit mTORC1 through a Rag-guanosine triphosphatase (GTPase)-dependent mechanism at the lysosome (Kalender et al., 2010). We reasoned that if phenformin inhibited mTORC1 by inhibiting lysosomal function, then mTORC1 would be insensitive to amino acid starvation if it was tethered to the lysosome, as shown in cells expressing FLAG-RAPTOR-RHEB15 (Sancak et al., 2010). In control cells that expressed FLAG-RAPTOR, chloroquine (CQ), a lysosome inhibitor, and phenformin both inhibited mTORC1 activity in response to amino acid stimulation (Figure S3A). However, in cells that express FLAG-RAPTOR-RHEB15, mTORC1 activity was protected from amino acid starvation in CQ-treated cells, as expected, but only partially protected by phenformin. Furthermore, phenformin inhibited mTORC1 in amino acid-starved FLAG-RAPTOR-RHEB15 cells that were co-treated with CQ, suggesting that a significant part of phenformin's action is independent of the lysosome (Figure S3A). In support of this conclusion, LC3-II or LC3B puncta did not accumulate in phenformin-treated cells (Figures 1A and 1D–1F) and lysosomal pH was unchanged by phenformin (Figure S3B).

Defects in Mitochondrial Complex I Suppress Autophagy

To determine whether phenformin's inhibition of autophagy was related to complex I inhibition, we measured autophagy in cells with genetic deletion of complex I accessory subunits whose importance in complex I assembly and activity was described by Stroud et al., (2016). We chose four knockout (KO) cell lines for these experiments: *NDUFS6*^{KO} and *NDUFS4*^{KO} lines, which are viable in galactose media and relatively competent in complex I assembly, and *NDUFA1*^{KO} and *NDUFA10*^{KO} lines, which are not viable in galactose

media and have severe defects in complex I assembly (Stroud et al., 2016). Basal mTORC1 activity appeared to be decreased in the KO cells, whereas AMPK activity was increased only in the cells with the more severe defect. In *NDUFS6*^{KO} and *NDUFS4*^{KO} cells, RB-induced autophagy was nearly as robust as autophagy in RB-treated control cells and was inhibited by phenformin to a similar degree (Figures 3A and S3C). In contrast, the amplitude of RB-induced autophagy was reduced in *NDUFA10*^{KO} and *NDUFA1*^{KO} cells and was not further decreased by the addition of phenformin (Figures 3A and S3C), suggesting that phenformin's inhibition of autophagy is primarily mediated by inhibition of complex I. BHMT fragmentation in vehicle-treated NDUF KO cells was less than in control cells (Figures 3A and S3C), suggesting that basal autophagy is suppressed by chronic defects in complex I.

Inhibition of complex I is reported to increase NADH and NADH/NAD+ ratios (Birsoy et al., 2015; Sullivan et al., 2015), and levels and metabolism of NAD+, the oxidized member of this redox pair, have been linked to the regulation of autophagy (reviewed in Jang et al., 2012). Therefore, we asked whether phenformin's inhibition of autophagy could be explained by changes in NADH/NAD+ ratios. We first determined that phenformin treatment increased the NADH/NAD+ ratio in HEK293 cells, which was largely reversed by the addition of mTOR inhibitors (Figure S3D). Although supplementation with nicotinamide (NM) to increase NAD+ biosynthesis decreased NADH/NAD+ ratios (Figure S3D), NM did not induce autophagy when used alone; it decreased RB-induced autophagy and did not rescue phenformin's inhibition of RB autophagy (Figures 3B and S3E). The lack of correlation between NADH/NAD+ ratios and autophagy suggests that increased NADH does not explain the autophagy defect associated with phenformin.

Finally, as with autophagy, RB-induced mitophagy was impaired in *NDUFA1*^{KO} cells compared to control cells (Figure 3C), without further inhibition by phenformin. Although CCCP did not induce measurable mitophagy in either cell line (Figure 3C), we could occasionally detect modest mitophagy in CCCP-treated HEK293 cells, but only at shorter time points (Figure S3F). PINK1 expression, although less robust in HEK293T cells compared to HEK293 cells, was not increased in vehicle-treated *NDUFA1*^{KO} cells (Figure 3C), suggesting that complex I defects do not activate PINK1-mediated mitophagy. Phenformin and CCCP both induced cleavage of the IMM GTPase optic atrophy 1 (OPA1), an energetic stress response that inhibits membrane fusion activity (Toyama et al., 2016), consistent with mitochondrial fragmentation (Figures S2A and S2B) (Veiga et al., 2018) and supporting the efficacy of phenformin in these cells. Altogether, these data show that defects in complex I and mitochondrial respiration suppress autophagy in higher eukaryotes, similar to what has been reported in yeast (Graef and Nunnari, 2011).

Phenformin and Glucose Starvation Increase AMP/ATP Energy Ratios and Cause Compensatory Metabolic Switching

The suppression of autophagy and mitophagy by phenformin led us to question whether there was sufficient energy in phenformin-treated cells to support autophagy. Although it is widely accepted that autophagy responds to energetic stress to increase survival (Meijer and Codogno, 2011), autophagy consumes ATP (Plomp et al., 1989), which suggests that cells

must maintain an energetic threshold to support autophagy. Adding adenosine to DMEM, which has been reported to increase ATP when used at millimolar concentrations (Li et al., 2013), significantly increased ATP levels in HEK293 cells (Figure S4A), decreased phosphorylation of ACC, and enhanced autophagy in response to mTOR inhibitors (Figure 4A) supporting the importance of ATP in fueling autophagy. To determine the energetic status of cells in conditions that induced or inhibited autophagy, we measured AMP/ATP energy ratios at 1, 6, and 24 hr in cells treated with RB and/or phenformin. For comparison, we included glucose-starved cells as an alternative means to induce energy stress. In RB-treated cells, the slight increase in the AMP/ATP ratio at 1 hr adjusted to control levels over time (Figure 4B). In contrast, AMP/ATP ratios in cells treated with phenformin or starved of glucose for 1 hr increased more than 25-fold (Figure 4B) with partial recovery over time, as cells presumably adjusted to the energetic stress by switching from OXPHOS to glycolysis, or vice versa. In support of such a switch, phenformin significantly increased lactate at 2 time points in both cells and media, decreased glucose levels, and depleted glycogen stores (Figures S4B–S4F), consistent with glucose consumption and a shift toward aerobic glycolysis. In contrast, lactate levels in glucose-starved cells were significantly decreased (Figure S4C), and the metabolites 3-hydroxyisobutyrate, 2-oxoisocaproate, and 3-methyl-2-oxovalerate were increased in cells and/or media (Figures S4G and S4H), consistent with the catabolism of branched chain amino acids BCAA to fuel the TCA cycle (Zhang et al., 2017). The metabolic changes in RB-treated cells more closely resembled glucose starvation than phenformin treatment (Figures S4B–S4E, S4G, and S4H). In phenformin-treated cells, the nearly complete recovery of AMP/ATP ratios at 6 hr was not lasting but instead increased again at 24 hr (Figure 4B), a rise that paralleled increasing phosphorylation of ACC (Figures 1A and4E).

Phenformin Suppresses the Initiation, Amplitude, and Duration of Autophagy

We predicted that if phenformin's inhibition of RB-induced autophagy was due to energy depletion, it was likely to occur at early time points when energy ratios were most severely affected. The WD-40 repeat domain phosphoinositide-interacting protein 2 (WIPI2) is a mammalian Atg18 ortholog that is recruited to early autophagosome structures, where it binds PtdIns3P, a product of VPS34/ATG14/BECLIN1 complex activity, and supports LC3 lipidation (Polson et al., 2010). We observed a decrease in WIPI2 puncta and the rate of LC3-II accumulation in RBP-treated cells, compared to RB treatment (Figures 4C, 4D, and S4H–S4K), suggesting that phenformin decreased early autophagosome formation. Despite this, there was little difference in the GST-BHMT fragment between cells treated with RB or RBP at 2 hr (Figures 4E and4F) or in SQSTM1/p62 levels (Figure 1D), suggesting that the decreased rate of autophagosome formation had little effect on the initial sequestration, delivery, or degradation of autophagy cargo. At subsequent time points, however, the amplitude of autophagy in RBP cells fell below that of RB-treated cells. Furthermore, in contrast to the stability of the GST-BHMT fragment in RB-treated cells (1A and4E), the reporter fragment in RBP-treated cells declined after 8 hr (Figures 4E and 4F). The fragment decay is consistent with attenuated autophagy and decreased cargo delivery; we could induce a similar decrease in BHMT fragment levels by treating cells 5 hr after the onset of autophagy with agents that disrupt vesicle trafficking or autophagosome and lysosome fusion (Figures S4M and S4N). We conclude that (1) although ATP clearly supports

autophagy, severe defects in energetic ratios do not prevent the initial sequestration of autophagic cargo induced by mTOR inhibitors, and (2) phenformin suppresses autophagy progression through a defect in autophagosome biogenesis.

Prolonged Glucose Starvation Increases Autophagy and Mitophagy

Although the effects of glucose starvation and phenformin on AMP/ATP ratios were similar, their effects on autophagy were different. In glucose-starved cells, GST-BHMT fragmentation and LC3-II levels, although initially unchanged, were increased at 24 hr (Figure 5A), consistent with reports that glucose starvation induces autophagy (Cheong et al., 2011; Kim et al., 2011). However, there was little correlation between the kinetics of AMPK activation, which occurred early, and the late induction of autophagy. In RB-treated cells, autophagy in glucose-depleted medium at early time points was comparable to autophagy in high-glucose DMEM but exceeded that of RB in high glucose at 24 hr and was stable up to 36 hr (Figures 5A, 5B, and S5A). Consistent with these findings, replacing glucose with either galactose, which provides no net ATP from aerobic glycolysis (Marroquin et al., 2007), or trehalose, a non-fermentable sugar that inhibits glucose transport (DeBosch et al., 2016), also increased autophagy and enhanced RB-induced autophagy (Figure 5C). It is likely that glucose-starved cells use TCA substrates like glutamine to support OXPHOS and survival (Wise and Thompson, 2010). Consistent with the importance of mitochondrial function for autophagy, supplementation of glucose-replete DMEM with the anapleurotic amino acids glutamine or aspartate increased the amplitude of RB-induced autophagy, although neither amino acid rescued the autophagy defect in cells treated with RBP (Figures S5B and S5C), consistent with a phenformin defect in complex I and OXPHOS. Finally, mitophagy in response to glucose starvation or galactose treatment was nearly as robust as mitophagy in RB-treated cells (Figure 5D) but was not observed in cells starved of essential amino acids (Figure S5D). We conclude that metabolic conditions that favor mitochondrial function and respiration also increase the amplitude of autophagy and mitophagy, independent of unfavorable AMP/ATP energy ratios.

Phospholipid Remodeling in Autophagy

The lack of correlation between energetic ratios and autophagy led us to consider phenformin's effects on phosphatidylethanolamine (PE) biosynthesis. Levels of lipidated LC3-II were often decreased in cells treated for 24 hr with phenformin (Figures 4E, 4G, 5D, and S5D), suggesting that phenformin may limit either the synthesis or the availability of PE, a phospholipid that is covalently attached to membrane-bound LC3 (Kabeya et al., 2004) and required for autophagy (Rockenfeller et al., 2015). Using targeted lipidomics, we found that phenformin alone had little effect on phospholipids, whereas RB significantly increased select species of PE and phosphatidylserine (PS) (Figures 6A, S6A, and S6B). PE (18:0/18:1) levels did not increase in cells treated with RBP, consistent with phenformin's inhibition of RB-induced autophagy. In mammalian cells, distinct pools of PE are synthesized on either mitochondria or endoplasmic reticulum (ER) membranes (Vance and Tasseva, 2013), and the mitochondrial phosphatidylethanolamine (mtPE) pool is reported to support autophagosome formation in starved cells (Hailey et al., 2010). To determine the importance of mtPE for RB autophagy, we measured autophagy in cells with 2 small interfering RNAs (siRNAs) targeting PISD, an IMM enzyme that converts PS to mtPE. Cells

with silencing phosphatidylserine decarboxylase (siPISD) were visibly stressed, with cleaved poly(ADP-ribose) polymerase 1 (PARP), indicative of early apoptosis, in siPISD-6 cells with the more severe knockdown (Figures 6B and S6C). These data are consistent with reports that loss of PISD causes defects in mitochondrial morphology and function, disrupts electron transport chain (ETC) complex formation, and is embryonic lethal in mice (reviewed in Vance and Tasseva, 2013). Basal autophagy was increased only in siPISD-6 cells, suggesting that the more severe PISD depletion induced a type of autophagy associated with apoptosis, a phenomenon also observed with the chemotherapy drug doxorubicin (Figure S6D). Despite this, the magnitude of RB-induced autophagy was decreased by knockdown of siPISD when compared to nonsilencing siRNA (siNS) control cells, and was further reduced by the addition of phenformin (Figure 6B). The latter suggests that complex I assembly was not fully compromised by partial PISD knockdown. To inhibit PISD more acutely, we used the PISD inhibitor hydroxylamine (Shiao et al., 1995; Voelker, 1993), which inhibited RB-induced autophagy without signs of apoptosis when used at 0.1 or 1 mM doses (Figure S6D). Others have shown that PISD activity is increased by exogenous serine (Shiao et al., 1995; Voelker, 1993), a non-essential amino acid that supports PS, sphingosine, and purine biosynthesis (Locasale, 2013). Adding serine to DMEM increased the amplitude of RB autophagy, which was reversed by the PISD inhibitor hydroxylamine (Figure 6C), supporting the importance of PISD activity and mtPE for autophagy. The addition of ethanolamine (ETN) to medium to favor ER biosynthesis of PE through the Kennedy pathway (Calzada et al., 2016) or mixed phospholipid liposomes also increased the amplitude of RB autophagy, although neither rescued the autophagy defect associated with phenformin (Figures 6D and S6F). We conclude that mTOR inhibitors enhance both phospholipid remodeling and autophagy that depends on PISD activity and mtPE, as well as that phenformin blocks the biosynthesis of mtPE.

Phenformin Blocks MAMs that Support Autophagy

We reasoned that phenformin might affect mtPE biosynthesis under autophagy-inducing conditions by limiting the availability of PS, the substrate for PISD (Di Bartolomeo et al., 2017). PS translocates from the ER to mitochondria at MAMs, which are regions of proximity between the ER and the mitochondria that support mitochondrial function (Naon and Scorrano, 2014) and autophagy, the latter through recruitment of ATG14 and VPS34 (Hamasaki et al., 2013). To determine the effect of our treatments on MAM formation, we used a proximity ligation assay with antibodies to inositol trisphosphate receptor (IP3R) and voltage-dependent anion channel (VDAC) on the ER and the OMM, respectively. We found that RB significantly increased the number of MAM contact sites compared to vehicle control (Figures 7A and 7B), consistent with the increase of WIPI2 puncta (Figures 4C and 4D), and autophagosome formation at MAMs (Hamasaki et al., 2013). Phenformin alone had little effect on MAM formation, but when combined with RB, it reduced the number of MAM contact sites compared to RB alone (Figures 7A and 7B). Moreover, MAMs did not increase in *NDUFA1*^{KO} cells treated with RB (Figures 7A and 7B), supporting the importance of complex I activity for autophagy. Finally, prolonged glucose starvation, which induced both a metabolic shift toward OXPHOS and autophagy (Figures 5, S5, and S4), increased MAM formation to levels equivalent to RB treatment (Figure S7), consistent with reports that MAM formation is sensitive to glucose availability (Theurey et al., 2016).

Altogether, these data support a model in which complex I activity is required to facilitate the transport of PS from the ER to mitochondria at MAMs, supplying PS substrate for the biosynthesis of mtPE and supporting both respiratory function and autophagy (Figure 7C).

DISCUSSION

Mitochondrial Metabolism Supports Autophagy

Understanding the relationship between autophagy and metabolism has previously focused on how autophagy fuels metabolism, supporting cell survival (Kimmelman and White, 2017). Our data demonstrate that a reciprocal relationship is also true, with metabolism regulating the amplitude of the autophagy response. We showed that a metabolic shift toward aerobic glycolysis decreased autophagy, whereas a shift toward OXPHOS increased the amplitude of autophagy, most strikingly in response to mTOR inhibitors. In the setting of cancer, the high metabolic demand of tumor cells, particularly those with activated RAS signaling, often depends on autophagy (Kimmelman and White, 2017), leading to clinical trials using lysosomal inhibitors to target autophagy directly and metabolism indirectly. Our data suggest that targeting mitochondrial OXPHOS for cancer therapy (Weinberg and Chandel, 2015) will inhibit both mitochondrial metabolism and autophagy.

Clinically, there is considerable interest in using metformin and phenformin for cancer treatment (Weinberg and Chandel, 2015), with nearly 100 actively recruiting clinical trials (https://clinicaltrials.gov/). Our data show that biguanides inhibit mTORC1 without the complication of activating autophagy and cause a metabolic shift toward glycolysis. We reported that the sequential use of phenformin and RB significantly prolonged survival in a mouse model of HCC, suggesting that phenformin metabolically sensitized HCC tumors to mTOR inhibitors (Veiga et al., 2018). It remains to be determined whether phenformin pretreatment blocked RB-induced autophagy *in vivo*, contributing to the efficacy of the combination. For tumors that are addicted to autophagy, the potential use of biguanides as autophagy inhibitors provides an alternative to CQ or hydroxychloroquine, without the disadvantages associated with profound lysosomal inhibition.

Complex I Defects Suppress Autophagy

We found lower basal autophagy in NDUF KO cells and an inverse correlation between the severity of the complex I defect and the amplitude of RB-induced autophagy. Mutations in each of the complex I assembly subunits used here have been implicated in Leigh syndrome, a pediatric mitochondrial disease marked by progressive neurodegeneration and early death (Rodenburg, 2016). Suppression of basal autophagy in mice with neuronal deletion of ATG5 was a contributing factor to their neurodegeneration (Hara et al., 2006), suggesting that defects in autophagy may contribute to the pathology of Leigh syndrome and other mitochondrial diseases. Rapamycin has been shown to slow disease progression in an *NDUFS4*$^{-/-}$mouse model of Leigh syndrome (Johnson et al., 2013) and in induced pluripotent stem cells (iPSCs) derived from a Leigh syndrome patient (Zheng et al., 2016). In the NDUF KO cells used here, RB treatment induced varying degrees of autophagy above basal levels, albeit lower than that of wild-type (WT) cells. It will be important to determine

whether more potent mTOR kinase inhibitors will provide an improved benefit in models of mitochondrial disease and whether autophagy and mitophagy are contributing factors.

AMP/ATP Energy Ratios, AMPK, and Autophagy

These data redefine how energetic stress affects autophagy, a dynamic program that requires energy for its execution (Meijer and Codogno, 2011; Plomp et al., 1989). A paradox of these studies is that RB-induced autophagy was amplified by both energy excess (adenosine) and energy deprivation (glucose starvation). Strategies to decrease ATP and activate AMPK did not acutely activate autophagy, although autophagy was measurably increased by prolonged glucose starvation. These data are consistent with those of Cheong et al. (2011), who argued that autophagy in response to glucose starvation is not due to bioenergetics failure but is instead caused by the accumulation of ammonia, an explanation that is consistent with much of our data. However, the finding that autophagy was increased when galactose was used as a carbon source argues for another mechanism, because galactose metabolism consumes ammonia but does not increase it (Roser et al., 2009). One explanation to resolve the energy and autophagy paradox is that cells that switch to, or enhance, mitochondrial OXPHOS increase ATP in a temporal and spatial manner at MAMs, where the ATPdependent processes of PS transport and autophagosome formation are active (Hamasaki et al., 2013; Shiao et al., 1995). This idea is supported by the presence of the ATP transporter VDAC at MAMs (Naon and Scorrano, 2014).

There was little correlation between acute AMPK activation and the late onset of autophagy in glucose-starved cells. Our data suggest that in cells with intact complex I function, mTOR inhibition is dominant in the acute activation of autophagy, whereas AMPK supports a second wave in a biphasic autophagy mechanism. The delayed effect could be explained by transcriptional changes (Pietrocola et al., 2013; Shin et al., 2016) or through the effects of increased β-oxidation, as suggested (Buzzai et al., 2005; Cheong et al., 2011). However, these effects do not explain the relevance of AMPK's acute phosphorylation of ULK1 that has been linked to autophagy (Egan et al., 2011; Kim et al., 2011). We propose that because ULK1 and ULK2 are dispensable for glucose starvation autophagy (Cheong et al., 2011), AMPK phosphorylation of ULK1/2 may be linked to either selective autophagy and/or metabolism. Consistent with this idea, Snf1 and Atg1, the yeast orthologs of AMPK and ULK1, control glycogen-specific autophagy (Wang et al., 2001), and the ULKs regulate glucose metabolic flux in starved cells independent of autophagy (Li et al., 2016). Additional studies are needed to more fully delineate the AMPK-ULK axis in glucose metabolism.

mTOR Inhibitors Increase Mitophagy

mTOR inhibitors and glucose starvation induced measurable and sustained mitophagy while preserving complex I activity, consistent with a report that mitophagy is induced by conditions that favor mitochondrial OXPHOS to optimize mitochondrial efficiency (Melser et al., 2013). In contrast, phenformin did not induce mitophagy, and the response to CCCP was nearly undetectable. Furthermore, mitophagy following prolonged CCCP treatment was lower than in vehicle-treated cells and comparable to levels found in *NDUFA1* KO cells, consistent with the idea that mitochondrial function and mitophagy are mutually dependent.

RB-induced mitophagy was independent of PINK1, which cooperates with PARKIN to remove damaged mitochondria. Mutations in PINK1 and PARKIN are associated with Parkinson's disease (PD), implicating defective mitophagy in disease pathogenesis (Pickrell and Youle, 2015). Our data suggest that the potent mitophagy induced by mTOR inhibitors could serve as a mitochondrial quality mechanism independent of PINK1/ PARKIN mitophagy for PD patients. Consistent with this idea, rapamycins have shown promise in models of PD and other neurodegenerative diseases (Bové et al., 2011). More potent mTOR kinase inhibitors may provide additional benefit for PD treatment, and their efficacy might be improved by metabolic strategies to amplify autophagy. Of these, trehalose and ETN have shown promise as agents to protect against aggregates associated with neurodegenerative disease or promote longevity (Rockenfeller et al., 2015; Sarkar et al., 2007). We hypothesize that complete inhibition of mTORC1 triggers selective mitophagy, just as it selectively regulates energetically costly biosynthetic pathways through post-translational modifications. This is consistent with the idea that mTORC1 coordinates both mitochondrial mass and protein synthesis to balance energetic output with demand (Morita et al., 2013).

MAMs and mtPE Play a Significant Role in Autophagy

PE is a positive regulator of autophagy (Rockenfeller et al., 2015); however, autophagy competes with other PE-consuming processes for the available phospholipid pool (Wilson-Zbinden et al., 2015), suggesting that PE is limiting for autophagy. mTOR inhibitors increased the abundance of select phospholipids, in correlation with increased autophagy. The increase in C18:0 and C18:1 phospholipid acyl chains are consistent with those identified in PE-lipidated Atg8 (Ichimura et al., 2000). We conclude, based on several pieces of evidence, that mtPE is the relevant species for autophagy. First, RB autophagy was suppressed by inhibiting PISD and increased with exogenous serine, which is purported to increase PISD activity (Shiao et al., 1995; Voelker, 1993). Serine and hydroxylamine may have other effects that are relevant for autophagy apart from PISD activity, requiring future work to validate their specific effects on mtPE biosynthesis in this context. Second, data showing that phenformin blocked the ability of ETN and phospholiposomes to increase RB-induced autophagy, and the RB-associated increase in MAMs, supports the importance of PS transport and substrate availability for PISD activity. This is related to PS transport being regulated by mitochondria respiration in yeast and mammalian cells (Miyata et al., 2016; Shiao et al., 1995). We propose that the increased autophagy observed with adenosine, glutamine, and aspartate is partly due to increased respiration, phospholipid transport, and mtPE biosynthesis. The possibility that PISD supports autophagy simply by promoting ETC activity cannot be ruled out. However, the increase in PE and autophagy, but not ATP, in cells treated with mTOR inhibitors, and the initiation of autophagy in energetically stressed cells, favors the importance of PISD-derived mtPE for autophagy. Future studies are needed to determine the physiological relevance of strategies that combine mTOR inhibition with manipulation of mtPE biosynthesis in pathologies in which autophagy is relevant. We are drawn to several hypotheses regarding how phenformin inhibits mtPE biosynthesis, each of which requires further investigation. First, mitochondrial fragmentation and the imbalance of fission to fusion may not be conducive to inter-organelle contact. The converse is true, because positive signals for autophagy, e.g., starvation or mTOR inhibitors, promote fusion, OXPHOS (Gomes et al., 2011; Veiga et al., 2018), and MAMs (data in this paper; Bravo-

Sagua et al., 2016; Theurey et al., 2016). Second, decreased respiration may change the expression of proteins required for PS transport, as shown in yeast (Miyata et al., 2016), or decrease the local availability of ATP for PS transport and MAM formation. Finally, we cannot rule out that post-translation modifications control MAM formation in a more acute manner. Altogether, these data demonstrate the dynamic and metabolic regulation of autophagy, highlighting the importance of mitochondrial complex I and respiration for a robust autophagy response.

STAR☆METHODS

Detailed methods are provided in the online version of this paper and include the following:

- KEY RESOURCES TABLE
- CONTACT FOR REAGENT AND RESOURCE SHARING
- EXPERIMENTAL MODEL AND SUBJECT DETAILS
  - Cell culture and experimental conditions
  - Cell lines used in this study
  - GST-BHMT and GST_{LSCS}GFP autophagy assays
  - GST_{LSCS}GFP-ActA mitophagy assay
  - LC3-II flux autophagy assay
  - LC3B and WIPI2 immunofluorescence
  - Live-cell confocal microscopy
  - Cell transfections of plasmids or siRNA
  - Complex I Enzyme Activity
  - Mitochondrial DNA content
  - Liposome preparation
  - Percoll density separation of mitochondria population
  - Quantitative Real-Time PCR
  - Lysosomal pH
  - Glycogen measurements
  - NAD+/NADH measurements
  - High performance liquid chromatography (HPLC) analysis of nucleotides
  - Proximity ligation assay (PLA) for MAMs
  - NMR Metabolomics analysis d
- QUANTIFICATION AND STATISTICAL ANALYSIS

- NMR Metabolomics Data analysis
- DATA AND SOFTWARE AVAILABILITY

KEY RESOURCES TABLE

REAGENT or RESOURCE	SOURCE	IDENTIFIER
Antibodies		
Rabbit Monoclonal pACC (Ser79)	Cell Signaling Technology	Cat# 11818; RRID: AB_2687505
Rabbit Monoclonal pS6K1 (Thr389)	Cell Signaling Technology	Cat# 9234; RRID: AB_2269803
Rabbit Monoclonal p4EBP1 (Ser65)	Cell Signaling Technology	Cat# 9456; RRID: AB_823413
Rabbit Polyclonal PARP	Cell Signaling Technology	Cat# 9542; RRID: AB_2160739
Mouse Monoclonal beta-actin	Cell Signaling Technology	Cat# 3700; RRID: AB_2242334
Mouse Monoclonal Myc-Tag (9B11)	Cell Signaling Technology	Cat# 2276; RRID: AB_331783
Rabbit Polyclonal pULK1 (Ser757)	Cell Signaling Technology	Cat# 6888; RRID: AB_10829226
Rabbit Monoclonal OPA1 (D6U6N)	Cell Signaling Technology	Cat# 80471; RRID: AB_2734117
Rabbit Monoclonal pAMPKa (Thr172)	Cell Signaling Technology	Cat# 2535; RRID: AB_331250
Rabbit Monoclonal TFAM (D5C8)	Cell Signaling Technology	Cat# 80761; RRID: AB_10949110
Rabbit Monoclonal PI3 Kinase Class III (D9A5)	Cell Signaling Technology	Cat# 4263; RRID: AB_2299765
Rabbit Monoclonal ATG14 (D1A1N)	Cell Signaling Technology	Cat# 96752
Rabbit Monoclonal ATG13 (D4P1K)	Cell Signaling Technology	Cat# 13273
Rabbit Monoclonal ATG101 (E1Z4W)	Cell Signaling Technology	Cat# 13492
Rabbit Monoclonal ULK1 (D8H5)	Cell Signaling Technology	Cat# 8054; RRID: AB_11178668
Rabbit Monoclonal ULK1 (D9D7)	Cell Signaling Technology	Cat# 6439; RRID: AB_11178933
Mouse Monoclonal Beclin-1 (2A4)	Cell Signaling Technology	Cat# 4122; RRID: AB_11178656
Mouse Monoclonal PARKIN Ab	Cell Signaling Technology	Cat# 4211; RRID: AB_2159920
Mouse Monoclonal S6K	BD Transduction Laboratories	Cat# 611261; RRID: AB_398791
Mouse Monoclonal GST (B-14)	Santa Cruz Biotechnology	Cat# sc-138; RRID: AB_627677
Mouse Monoclonal TOM20 (F-10)	Santa Cruz Biotechnology	Cat# sc-17764; RRID: AB_628381
Mouse Anti-p62 lck ligand (SQSTM1)	BD Biosciences	Cat# 610832; RRID: AB_398151
Rabbit Polyclonal LC3B	Novus Biologicals	Cat# NB100–2220; RRID: AB_10003146
Rabbit Polyclonal LC3B	Abcam	Cat# ab51520; RRID: AB_881429

REAGENT or RESOURCE	SOURCE	IDENTIFIER
Rabbit Polyclonal PINK1	Novus Biologicals	Cat# BC100–494; RRID: AB_10127658
Rabbit Polyclonal RB1CC1 (FIP200)	Novus Biologicals	Cat# NB100–77279; RRID: AB_1085475
Rabbit Polyclonal RRBP1	Bethyl	Cat# A303–996A; RRID: AB_2620345
Mouse Monoclonal VDAC1	Abcam	Cat# ab14734; RRID: AB_443084
Rabbit Polyclonal IP3 Receptor	Abcam	Cat# ab5804; RRID: AB_305124
Mouse Monoclonal anti-FLAG M2	Sigma	Cat# F1804; RRID: AB_262044
Mouse Monoclonal Cytochrome Oxidase Subunit II (COX II)	Molecular Probes	Cat# A6404; RRID: AB_221584
CoralHue Keima-Red Mouse Monoclonal Antibody	MBL International	Item# M126–3M 013; RRID: AB_843710
Rabbit Polyclonal WIPI2 antibody	Invitrogen	Cat# PA5–54098; RRID: AB_2649654
Goat anti-rabbit IgG, Alexa Fluor 488 secondary antibody	Invitrogen	Cat# A11008; RRID: AB_143165
Goat anti-mouse IgG, Alexa Fluor 680 secondary antibody	Invitrogen	Cat# A21057; RRID: AB_2535723
IRDye 680RD Goat anti-mouse	LiCOR	Cat# 926–68070; RRID: AB_10956588
IRDye 800 CW Goat anti-rabbit	LiCOR	Cat# 926–32211; RRID: AB_621843
Chemicals, Peptides, and Recombinant Proteins		
Everolimus (RAD001)	LC laboratories	Cat# E4040
NVP-BEZ235	LC laboratories	Cat# N4288
Phenformin hydrochloride (P)	Sigma-Aldrich	Cat# P7045
Dextrose (Gluc)	Sigma-Aldrich	Cat# D9434
D-Galactose (Gal)	Calbiochem	Cat# CAS 59–23-4
L-Aspartic acid (Asp)	Sigma-Aldrich	Cat# A7219
L-Glutamine (Gln)	Sigma-Aldrich	Cat# G8540
L-Serine	Sigma-Aldrich	Cat# S4311
D-Trehalose dihydrate (Treh)	Sigma-Aldrich	Cat# T0167
Adenosine	Sigma-Aldrich	Cat# A4036
Nicotinamide (NM)	Sigma-Aldrich	Cat# N0636
FK866 hydrochloride hydrate (FK)	Sigma-Aldrich	Cat# F8557
Carbonyl cyanide 3-chlorophenyl-hydrazone (CC)	Sigma-Aldrich	Cat# C2759
Chloroquine diphosphate salt (CQ)	Sigma-Aldrich	Cat# C6628
1,1-Dimethylbiguanide hydrochloride (Metformin) (M)	Aldrich	Cat# D15,095–9
Ethanolamine (ETN)	Sigma-Aldrich	Cat# 15014
Uridine	Sigma-Aldrich	Cat# U3003
Hydroxylamine solution	Sigma-Aldrich	Cat# 467804
Antimycin A	Sigma-Aldrich	Cat# A8674

REAGENT or RESOURCE	SOURCE	IDENTIFIER
Oligomycin A	Sigma-Aldrich	Cat# 75351
Rotenone	Sigma	Cat# R-8875
Leupeptin hemisulfate	Bacham	Cat# N-1000
E64d	Bacham	Cat# N-1650
Vinblastine (Vin)	Sigma-Aldrich	Cat# V1377
Nocodozole (Noc)	Sigma-Aldrich	Cat# M1404
Bafilomycin A1 (Baf)	Sigma-Aldrich	Cat# B1793
Doxorubicin hydrochloride	Sigma-Aldrich	Cat# PHR1789
Percoll	Sigma-Aldrich	Cat# P1644
L-alpha-phosphatidylserine (PS)	Avanti	Cat# 840032C
L-alpha-phosphatidylcholine (PC)	Avanti	Cat# 840051C
L-alpha-phosphatidylethanolamine (PE)	Avanti	Cat# 841118C
Critical Commercial Assays		
RNeasy Mini Kit	QIAGEN	Cat# 74104
DNeasy Blood & Tissue Kit	QIAGEN	Cat# 69506
QuantiNova SYBR Green PCR Kit	QIAGEN	Cat# 208052
RT2 qPCR Primer Assay (ACTIN, PISD, TFAM, PPARG1alpha, and NRF1)	QIAGEN	Cat# 330001
SuperScript III First-Strand Synthesis SuperMix for qRT-PCR	Invitrogen	Cat# 11752–050
Fast SYBR Green Master Mix	Applied Biosystems	Cat# 4385612
Duolink In Situ PLA Probe Anti-Rabbit PLUS	Sigma-Aldrich	Cat# DUO92002
Duolink In Situ PLA Probe Anti-Mouse MINUS	Sigma-Aldrich	Cat# DUO92004
Duolink In Situ Detection Reagents Red	Sigma-Aldrich	Cat# DUO92008
Mitochondria Isolation Kit for Cultured Cells	Abcam	Cat# ab110170
Complex I Enzyme Activity Microplate Assay Kit	Abcam	Cat# ab109721
Glycogen Assay Kit	Abcam	Cat# ab65620
NAD/NADH Quantitation Colorimetric Kit	BioVision	Cat# K337
LysoSensor Yellow/Blue Dextran	Molecular Probes	Cat# L22460
Lipofectamine 3000 transfection kit	Invitrogen	Cat# L3000015
FuGENE 6 transfection reagent	Promega	Cat# E2691
Pierce glutathione agarose	Thermo Scitific	Prod# 16100
Vectashield mounting medium with DAPI	Vector Laboratories	Cat# H-1200
RIPA lysis buffer	EMD Millipore	Cat# 20–188
Deposited Data		
NMR and LIpidomics data	This paper	https://doi.org/10.17632/ccx58pdy3d.1
Experimental Models: Cell Lines		
HEK293 (human, embryonic kidney)	ATCC	Cat# CRL-1573, RRID:CVCL_0045
HEK293T (human, embryonic kidney)	Laboratory of Michael T Ryan	(Stroud et al., 2016)

REAGENT or RESOURCE	SOURCE	IDENTIFIER
		RRID:CVCL_0063)
HEK293T NDUFA1 KO	Laboratory of Michael T Ryan	(Stroud et al., 2016)
HEK293T NDUFA10 KO	Laboratory of Michael T Ryan	(Stroud et al., 2016)
HEK293T NDUFS4 KO	Laboratory of Michael T Ryan	(Stroud et al., 2016)
HEK293T NDUFS6 KO	Laboratory of Michael T Ryan	(Stroud et al., 2016)
HEK293 TOMM20-Keima	Laboratory of J. Wade Harper	(An and Harper, 2018)
HEK293 TOMM20-Keima with PARKIN overexpression	Laboratory of J. Wade Harper	(An and Harper, 2018)
HEK293 Mito-Keima	Laboratory of J. Wade Harper	(An and Harper, 2018)
HEK293T Flag-RAPTOR	Laboratory of G. Thomas	N/A
HEK293T Flag-RAPTOR-RHEB15	Laboratory of G. Thomas	N/A
A549 (human, male, lung epithelial carcinoma)	ATCC	Cat# CCL-185, RRID:CCVL_0023
Hep3b (human, male, hepatocellular carcinoma)	ATCC	Cat# HB-8064. RRIC:CCVL_0326
H9C2 (2–1) (rat, embryonic)	ATCC	Cat# CRL-1446, RRID:CVCL_286
Oligonucleotides		
FlexiTube siRNA Hs_PISD_6	QIAGEN	Cat# SI04201750
Sense 5’-GCGUCGUGUGACUCCUUCATT-3’		
Anti 5’-UGAAGGAGUCACACGACGCGG-3’		
FlexiTube siRNA Hs_PISD_7	QIAGEN	Cat# SI04249182
Sense 5’-GAUUAAUGAUACAGACCUUTT-3’		
Anti 5’-AAGGUCUGUAUCAUUAAUCAG-3’		
GAPDH gDNA	IDT	(Prabhu et al., 2013)
Forward 5’-CCCCACACACATGCACTTACC-3’		
Reverse 5’-CCTAGTCCCAGGGCTTTGATT-3’		
b-Actin gDNA	IDT	(Prabhu et al., 2013)
Forward 5’-TCACCCACACTGTGCCCATGTACGA-3’		
Reverse 5’-CAGCGGAACCGCTCATTGCCAATGG-3’		
ATPase8 mtDNA	IDT	(Prabhu et al., 2013)
Forward 5’-AATATTAAACACAAACTACCACCTACC-3’		
Reverse 5’-TGGTTCTCAGGGTTTGTTATA-3’		
hCytochrome b mtDNA	IDT	(Morita et al., 2013)
Forward 5’-GCGTCCTTGCCCTATTACTATC-3’		
Reverse 5’-CTTACTGGTTGTCCTCCGATTC-3’		
Recombinant DNA		
GST-BHMT-IRES-GFPmyc (pRK5)	Laboratory of C. Mercer and P. Dennis	Addgene plasmid #104442

REAGENT or RESOURCE	SOURCE	IDENTIFIER
GSTLCSCGFP-ActA (pRK5)	Laboratory of C. Mercer and P. Dennis	Addgene plasmid #104452
GSTLCSCGFP (pRK5)	Laboratory of C. Mercer and P. Dennis	Addgene plasmid #104451
FLAG-RAPTOR (pLJM1)	A gift from D. Sabatini	Addgene plasmid #26633
FLAG-RAPTOR-RHEB15 (pLJM1)	A gift from D. Sabatini	Addgene plasmid #26634
Software and Algorithms		
Fiji ImageJ	https://imagej.net/Fiji	N/A
GraphPad Prism 7	GraphPad software	N/A
Topspin 3.1, Bruker Analytik, Rhenstetten, Germany	https://www.bruker.com/products/mr/nmr/nmr-software/nmr-software/topspin/overview.html	N/A
Chenomx NMR Suite profiling software, Chenomx Inc. version 8.1	https://www.chenomx.com/	N/A

CONTACT FOR REAGENT AND RESOURCE SHARING

Further information and requests for resources and reagents should be directed to and will be fulfilled by the Lead Contact, Carol A. Mercer (mercerc@ucmail.uc.edu).

EXPERIMENTAL MODEL AND SUBJECT DETAILS

Cell culture and experimental conditions—All cells were cultured at 37°C, in 5% CO_2, in DMEM containing essential and non-essential amino acids, 4 mM glutamine, 1 mM sodium pyruvate, and 10% fetal calf serum (FCS). Experiments with glucose or amino acid starvation, galactose, or trehalose contained FCS dialyzed extensively against 25 mM HEPES pH 7.3, 50 mM NaCl, using Spectra/Por membrane with MWCO 3500 (Spectrum Labs).

Cell lines used in this study

- HEK293 cells (human, sex unknown, embryonic kidney, ATCC CRL-1573, RRID:CVCL_0045)
- HEK293 Keima knock-in cells were generously provided by J. Wade Harper (An and Harper, 2018).
- HEK293T cells (human, sex unknown, embryonic kidney, RRID:CVCL_0063)
- HEK293T cells with genetic deletion of *NDUFA1*, *NDUFA10*, *NDUFS4* and *NDUFS6* were cultured in DMEM supplemented 50 μg/ml uridine. Uridine was added to DMEM for both HEK293T parental and KO cells under experimental conditions. These cells were generously provided by Michael T. Ryan (Stroud et al., 2016).
- For experiments in HEK293T cells that stably express Flag-RAPTOR and Flag-RAPTOR-RHEB15, cell media was refreshed with a half media change 6 h before treatment. At time zero, cells were placed in DMEM with 25 mM

glucose, 1 mM pyruvate and 4 mM glutamine, but without essential amino acids or serum for 60 minutes. For amino acid stimulation, a mix of essential amino acids (EAA) was added during the last 10 minutes, for final EAA concentrations equal to 1x DMEM.

- A549 cells (human, male, lung epithelial carcinoma, ATCC CCL-185, RRID:CVCL_0023)
- Hep3b cells (human, male, hepatocellular carcinoma, ATCC HB-8064, RRID:CVCL_0326)
- H9C2 (2–1) cells (rat, embryonic myoblast, ATCC CRL-1446, RRID:CVCL_286)

GST-BHMT and GST_{LSCS}GFP autophagy assays—The GST-BHMT and GST_{LSCS}GFP assays were performed as previously described (Dennis and Mercer, 2009; Mercer et al., 2008). In brief, cells expressing GST-BHMT-IRES-GFPmyc, GST_{LSCS}GFP, or GST_{LSCS}GFP-ActA were cultured for the times indicated, with drugs or treatments as described. 5 nM RAD001 and 20 nM BEZ235 served as a positive control to induce autophagy/mitophagy. Leupeptin (11 μM) and E64d (6 μM) were added at the beginning of each treatment. The following steps were performed on ice or at 4°C. Except for Figure S4B, which were harvested for light membrane fractions (LMFs) or unless otherwise indicated in the Figure panel, cells were harvested in extraction buffer (EB) with 1% Triton X-100 (EB-TX) (50 mM TRIS-HCl pH 8, 120 mM NaCl, 5 mM NaPPI, 10 mM NaF, 30 mM para-nitrophenylphosphate, 1 mM benzamidine, 0.2% NP-40 and fresh 0.2 mM PMSF). Total protein was determined by the Bradford method; and GST-BHMT was precipitated with glutathione agarose from 300–400 μg of cell lysate. Bound GST-proteins were washed once in EB with 500 mM NaCl, and 1–2 times in wash buffer (50 mM MOPS pH 7.5, 10 mM NaF, 30 mM β-gycerolphosphate, 1 mM DTT, 0.1% Triton X-100, 10% glycerol). Precipitates were boiled in SDS-PAGE sample buffer, eluted, resolved by SDS-PAGE, followed by western blotting and imaging with the Odyssey system. Whole cell lysates (25–30 μg) were resolved by SDS-PAGE, followed by western blotting and imaging with the Odyssey system, and probed for antibodies as described. Western blotting for GFP-myc, whose expression is under the control of an internal ribosome entry site (IRES), was used to normalize expression of the GST-BHMT-IRES-GFPmyc plasmid. The GST-BHMT fragment and GFP myc densities were quantified using the LiCOR imaging software, and the GST-BHMT frag/GFP ratio was calculated as an autophagy index. Raw ratios are shown on all graphs, whereas the numerical autophagy “index” is shown on western blots, with normalization to the RB GST-BHMT frag/GFP ratio represented as 1.0.

GST_{LSCS}GFP-ActA mitophagy assay—The GST_{LSCS}GFP-ActA mitophagy assay was performed as previously described (Dennis and Mercer, 2009) from LMFs. All steps were performed on ice or at 4°C. PBS-washed cells were collected and centrifuged at 1000xg for 5 min; the cell pellet was suspended in 400–500 μl homogenization buffer (HB) (10 mM TRIS pH 7.5, 300 mM sucrose, 0.2 mM EDTA, 0.2 mM PMSF) and disrupted by Dounce homogenization for 10–15 strokes. The homogenate was centrifuged at 540 xg and the supernatant was collected. The homogenization step was repeated with the low speed pellet,

and the combined supernatant was centrifuged at 12,000 xg for 20 min to separate the LMF in the pellet from the high-speed supernatant (HSS). The LMF fraction was homogenized in EB-TX, LMF protein was determined by Bradford method, and GST-tagged proteins were precipitated with glutathione agarose from 50 or more ug of LMF extract. Bound GST proteins were washed, boiled in SDS-sample buffer, eluted, resolved by SDS-PAGE and visualized as described above. 10 μg of LMF extract was resolved by SDS-PAGE, followed by western blotting for mitochondria and autolysosomal proteins as described.

LC3-II flux autophagy assay—Cells were pre-treated for 1h with drugs as described, then treated with 100 μM chloroquine (CQ), and harvested after 40 minutes. The time of harvest was based on preliminary time course studies to determine the optimal time to capture differences between control and autophagy inducing conditions. Cells were harvested in EB-TX, total protein was determined by Bradford assay, and 25 μg of total extract was resolved by SDS-PAGE, followed by western blotting for LC3, and other proteins as described. For LC3-II rate analysis, cells were treated as described above with drugs and CQ, and cells were harvested at time points as described. In both assays, levels of LC3-II were normalized to ACTIN.

LC3B and WIPI2 immunofluorescence—HEK293 cells were seeded on 35 mm coverslip collagen coated dishes (MatTek), grown to ~65%–70% confluency. For LC3B puncta, cells were treated as described for the LC3-II flux assay. For WIPI2 puncta, cells were treated for 2 h. Cells were washed with PBS, fixed with ice cold methanol, rinsed x3 with PBS, permeabilized with 0.1% saponin in PBS, blocked with 1% BSA, 0.1% saponin in PBS, and incubated for 1 h with Abcam anti-LC3B antibody (1:5000), or anti-WIPI2 antibody (1:200), at 37C in a humidity chamber. Cells were rinsed x3 with PBS, incubated with a goat anti-rabbit Alexa Fluor 488 secondary antibody (1:1000) diluted in blocking solution, rinsed, dried and coverslipped with mounting media. 6–10 z stack images were captured for each treatment, using a Zeiss Axio Observer Z1 inverted microscope, 63x oil immersion lens (1x zoom), connected to a Zeiss LSM710 confocal, and analyzed with Fiji ImageJ (https://imagej.net/Fiji).

Live-cell confocal microscopy—HEK293 cells were seeded on 35 mm coverslip collagen coated dishes (MatTek), cultured to ~60% confluency, and duplicate plates were treated for ~4 h with V, RB, P^1 or RBP^1. Z stack images of live cells were acquired with a Zeiss LSM710 confocal with a Zeiss Observer.Z1 stand and a Zeiss Plan-Apochromat 63x/1.4 objective with a stage incubator maintained at 37°C. Mito-Keima fluorescence was measured from 600–740nm upon excitation with a 458nm or 561nm laser respectively. Images were analyzed with Fiji ImageJ (https://imagej.net/Fiji). Experiment was performed a minimum of 2 times.

Cell transfections of plasmids or siRNA—The optimal method for transfection of each cell line was determined experimentally. HEK293 and 293T cells were transfected by the calcium phosphate method (Chen and Okayama, 1988), using sterile filtered 2X BBS (50 mM BES, 280 mM NaCl, 1.5 mM Na_2HPO_4) pH ~7 and 20X 2.5 M $CaCl_2$ prepared in

house. A549 and H9c2 cells were transfected with Lipofectamine 3000, and Hep3b cells with Fugene 6, following manufacturers' protocols.

Complex I Enzyme Activity—Mitochondrial complex I activity was measured using the Abcam Complex I Enzyme Activity Kit (ab109721) per manufacturer's directions. HEK293 cells were seeded at ~5.5 3 10^6 cells per 15 cm dish (n = 16) to reach ~70% confluency at 48 h. Cells were then treated for a minimum of 16 h with V, P^1, RB or RBP^1 (4 plates each). At harvest time, cells were washed twice with ice cold PBS, scraped into PBS, and pelleted at 1000 xg. 5% was reserved for further protein analysis, and the remainder was used for isolation of mitochondria, using either the LMF protocol, or Abcam Mitochondria Isolation Kit. Purified mitochondria were suspended in 500 μl Buffer C and lysed for 30 min with detergent (1% lauryl maltoside, final concentration). After centrifugation, mitochondrial protein was quantified by Bradford and mitochondrial lysates were adjusted to the same mg/ml concentration. Serial dilutions were prepared in incubation solution (Abcam CI Assay Kit). Complex I activity in 200 μl was measured on serial dilutions, each in triplicate, per manufacture's protocol, using a Molecular Devices VERSAmax microplate reader at 450nm, with kinetic readings taken every 30 s for 30 minutes. Activity is represented as mOD/min. The assay shown is representative of 4 independent experiments, with 2 or more dilutions.

Mitochondrial DNA content—Mitochondrial DNA content was determined using a quantitative real-time PCR approach, as described (Venegas and Halberg, 2012). In brief, 10 sets of HEK293 cells were treated for 24h with V, RB, P^1, and RBP. Total DNA from each plate was isolated using the QIAGEN DNeasy Blood and Tissue Kit according to manufacturer's protocol, and quantified using a NanoDrop 2000c (Thermo Scientific). Four random sets of DNA were selected for qPCR on an Applied Biosystems 7500 Fast Real-Time PCR System, using Fast SYBR Green Master Mix, and 2 nuclear (n) primer sets against *nGAPDH* and *nACTIN* and 2 mitochondrial (mt) primer sets against mt*ATPase8* and mt*CYTOCHROME b* (Morita et al., 2013; Prabhu et al., 2013) (See Key Resources Table). Ct values were determined for each sample in quadruplicate, and ΔCt values were determined for each nuclear-mitochondria pair (n*GAPDH* Ct – mt*Cytb* Ct) and (n*ACTIN* Ct – mt*ATPase8* Ct). Mitochondrial DNA content for each nuclear-mitochondria pair was determined using the formula 2×2(ΔCt), and averaged. The experiment was repeated using 4 additional sets of DNA.

Liposome preparation—Liposomes were prepared with L-α-phosphatidylserine (PS) (brain, porcine), L-α-phosphatidylcholine (PC) (egg, chicken), and L-a-phosphatidylethanolamine (PE) (egg, chicken), each initially obtained as a 10 mg/mL stock solution in chloroform ($CHCl_3$). Suspensions of liposomes in HEPES buffered saline (HBS) (20 mM HEPES, 100 mM NaCl, pH 7.4) with total lipid concentrations of 1 mM were prepared with variable molar ratios of PC, PS, and PE: (a) 8:2:0 PC/PS/PE (mol/mol/mol), (b) 6:2:2 PC/PS/PE (mol/mol/mol), or (c) 4:2:4 PC/PS/PE (mol/mol/mol). The lipid solutions in $CHCl_3$ were mixed and then dried under $Ar_{(g)}$. HBS was added to the dried lipid film, incubated (1 h, 22°C), and vortexed (3 3 30 s, 22°C). The diameter of the resultant liposomes was reduced by sequential extrusion through a 200-nm and 100-nm polycarbonate

membrane filters (Avanti Cat #s 610006 and 610005). The liposomes were briefly stored on ice prior to use.

Percoll density separation of mitochondria population—Crude mitochondria were isolated and separated by density as previously described (Wieckowski et al., 2009). Starting number of HEK293 cells was ~150–200 × 10^6 per treatment group, following 4 h treatments as described in text. Briefly, cells were washed and collected in PBS, disrupted by dounce homogenization in buffer (225 mM mannitol, 75 mM sucrose, 0.1 mM EGTA, 30 mM Tris-HCL pH 7.4), and crude mitochondria were isolated by multiple centrifugation steps. Mitochondria protein concentrations were measured by Bradford. 2 mg of mitochondria protein were loaded on a 30% Percoll gradient and centrifuged in an SW-41 rotor for 35 min, 95,000 g, to separate mitochondria into light and dense fractions. Each fraction was collected, diluted in mitochondria resuspending buffer (250 mM mannitol, 5 mM HEPES (pH 7.4) and 0.5 mM EGTA), and centrifuged at 6,300 g for 10 min. Pellets were washed, recentrifuged as before, and resuspended in equal volumes. 10 ug of crude mitochondria and a percentage of recovered fractions were separated by SDS-PAGE, with western blotting for proteins as shown.

Quantitative Real-Time PCR—RNA was isolated from triplicate plates of HEK293 cells transfected with siNS, siPISD-6 and siPISD-7, using the QIAGEN RNeasy kit per manufacturer's instructions. For qRT-PCR of PGC1a, NRF1 and TFAM, HEK293 cells were treated for 24 h with V, RB, P^1, or RBP^1, prior to RNA isolation. 500 ng of total RNA was used for reverse transcription using Invitrogen Superscript III First Strand Synthesis SuperMix. mRNA gene expression was determined using QuantiNova SYBR Green PCR Kit on the Applied Biosystems 7500 Fast Real-Time PCR System, per manufacturer's instructions, with normalization to ACTIN. RT^2 qPCR primer assays for ACTIN, PISD, NRF1, PPARGα (PGC1α), and TFAM used in qRT-PCR reactions were purchased from QIAGEN.

Lysosomal pH—Lysosomal pH was measured using LysoSensor Yellow/Blue dextran (Molecular Probes) per recommended protocol. HEK293 cells were treated for ~4.5 h with V, RB, P^1, or RBP^1. Cells were washed with PBS, trypsinized, centrifuged and resuspended in DMEM. Cells were counted using Trypan Blue and the Invitrogen Countess Cell Counting chamber system and adjusted to 1 × 10^6 cells/ml. 1 mL cell aliquots were pelleted by centrifugation, and pellets were resuspended in ~50 μl residual DMEM. 50 μl of 2 mg/ml Yellow/ Blue dextran in DMEM was added to each cell pellet for a final concentration of 1 mg/ml dextran, excluding a no-dextran control, which received DMEM only. Cells were incubated for 2 h at 37°C, 5% CO2, washed × 3 with Hank's buffered salt solution (HBSS), and resuspended in 1 mL HBSS. Samples (100/well) were loaded on a black 96-well plate (8 wells per each) and fluorescence was monitored using a Clariostar microplate reader with emission wavelengths at 452 nm and 521 nm, and excitation at 335 nm. The ratio of emissions at 452/521 nm was calculated for each sample, and pH values were calculated from a linear calibration curve. The calibration curve was generated by incubating cells for 10 min at 37°C, prior to dextran loading, with 10 uM monensin and 10

uM nigericin in MES buffers (5 mM NaCl, 115 mM KCL, 1.3 mM MgSO4, 25 mM MES), with pHs ranging from 3.5 – 7.0 (Diwu et al., 1999). $r^2 = 0.913$

Glycogen measurements—3.5×10^5 HEK293 cells were plated in 6-well dishes and grown to ~60%–70% confluence. Cells were treated in triplicate for 6 h with V, RB, P^1 or RBP^1. Glycogen measurements were performed in triplicate with 3 separate dilutions, using Abcam's Glycogen Assay kit per manufacturer's instructions. Glycogen levels were determined using a freshly prepared standard curve: slope = 0.6074, $r^2 = 0.9990$.

NAD+/NADH measurements—1.7×10^5 HEK293 cells were plated in 6-well dishes and grown to ~50%–60% confluence. Cells were treated in duplicate for 6 h with V, RB, P^1, RBP^1, 5 mM NAM, 10 nM FK866, or RBP+NAM and harvested and analyzed for NADH and NAD+ using the BioVision NAD/NADH Quantitation Colorimetric Kit per manufacturer's instructions. In brief, cells were washed in cold PBS and scraped into 400 µl cold extraction buffer and disrupted by dounce homogenization (10 strokes), vortexed 10 s, and centrifuged at 4°C for 5 min. Half of the supernatant was heated for 30 min at 60°C to decompose NAD, leaving NADH intact (NADH), and quick spun to remove any precipitates. The remaining half contained total NAD and NADH (NADt). 50 µl of each undiluted sample (total or heated), and each sample diluted 1:2 and 1:4, was immediately assayed in duplicate in 96-well format. NAD Cycling Mix (100 µl/well) was added, mixed and incubated for 5 min at RT to convert NAD to NADH, and then 10 µl of NADH developer was added for 1–4 h, and the plate was read at OD 450 nm after the reactions were stopped with Stop Solution (10 µl). Ratios were calculated as NADH / NADt – NADH.

High performance liquid chromatography (HPLC) analysis of nucleotides—HEK293 cells were plated on 10cm dishes, treated as described in text, and harvested at the times indicated in duplicate. Cells were rinsed 2 times with cold PBS, scraped into 1ml of 80% acetonitrile, and centrifuged at 4°C for 5 min. Supernatants were heat shocked at 80°C for 3 min, speed vacuumed until dry, and rehydrated with 100–200 µl HPLC water. Following centrifugation, samples were analyzed by HPLC on a Shimadzu LC-10AT *VP* system with a ZORBAX Extend-C18 column (Agilent). Analyses were performed using a sample injection volume of 50 µl at room temperature (RT), a flowrate of 1.0 ml/min, and a linear gradient program. Buffer A: 20 mM NaH_2PO_4 pH 8.5 with NaOH, 10 mM tetrabutyl ammonium hydrogen (TBA); Buffer B: 100 mM NaH_2PO_4 pH 3.0 with HCl, 10 mM TBA, 30% MeOH; Buffer C: 30% MeOH. The HPLC program was: 0–15 min, 0%B, 0%C; 20 min, 10%B, 0%C; 25min, 15%B, 0%C; 65min, 30%B, 0%C; 85 min, 60%B, 0%C; 95 min, 80%B, 0%C; 95.1 min, 0%B, 100%C; 120 min, 0%B, 100%C; 121 min, 0%B, 0%C; 130 min, stop. UV detection was set at 254 nm wavelength. Peaks were identified by retention times and compared to the peak spectrum of authentic standards. For ATP analysis in cells supplemented with adenosine, HPLC protocol was modified as follows: (i) samples were injected at a volume of 60 ul; (ii) Buffer C was not included, and (iii) program details were 0–20 min, 0%B; 25 min, 15%B; 40 min, 55%B; 70 min, 30%B; 85 min, 60%B; 95 min, 80%B; 110 min, 80%B; 115 min, 0%B; 120 min, stop.

Proximity ligation assay (PLA) for MAMs—The PLA for MAMs followed a previously described protocol (Tubbs and Rieusset, 2016) and the DuoLink InSitu Detection Reagents Red kit instructions (Sigma). 1.3–1.6 × 10^5 HEK293T and 1.5–2.2 × 10^5 *NDUFA1*^{KO} cells were seeded on 35 mm coverslip collagen coated dishes (MatTek), cultured to ~60% confluency, and duplicate plates were treated for 4h with V, RB, P^1 or RBP. Control plates for no antibody or single antibodies were treated with V. Cells were washed with PBS and fixed for 10 min at RT with fresh 4% formaldehyde solution in PBS (Thermo Scientific Pierce, #28908), which was stopped by adding an equal volume of 1M glycine. Cells were washed once with PBS, and incubated in 100 mM glycine for 15 min at RT, permeabilized with 0.1% Triton X-100 in PBS for 15 min at RT, washed once with PBS, and blocked for 30 min at 37°C in a humidity chamber with blocking reagent (included in the DuoLink InSitu PLA Probe kit). Anti-IP3R-1 (rabbit) and anti-VDAC1 (mouse) antibodies were prepared at 1:500 and 1:100 dilutions respectively, and added to cells for overnight incubation, in a humidity chamber at 4°C. Plates were washed twice with TBS-Tween (0.01%) or DuoLink Fluorescent Wash buffer A, then incubated for 1h at 37°C in a humidity chamber with DuoLink InSitu PLA Probes, Anti-Rabbit Plus and Anti-Mouse Minus. The ligation and amplification steps, with their incubation times, conditions, and wash steps were performed per manufacturer's instructions. After the final washes in 1x and 0.01x DuoLink Fluorescent Wash buffer B, plates were dried and then mounted with round coverslips using aqueous mounting media with DAPI (Vector Labs). A minimum of 10 z stack images were captured for each cell line and treatment, using a Zeiss Axio Observer Z1 inverted microscope, 63x oil immersion lens (1x zoom), connected to a Zeiss LSM710 confocal and analyzed with Fiji ImageJ (https://imagej.net/Fiji). Images shown are maximal projection images. Data are representative of 3 independent experiments in WT and NDUF KO cells, and 2 independent experiments with glucose starvation.

Targeted phosphatidylethanolamine (PE) and Phosphatidylserine (PS) analysis: Quantitative analysis of PE and PS was carried out using a Waters Premier XE triple quadrupole mass spectrometer interfaced with an Acquity ultra-high performance liquid chromatography (UPLC) system (Waters, Milford, MA). Mass spectrometer was operated in electrospray ionization mode with negative ion acquisition. Phospholipids were extracted from cells by the Folch procedure with initial addition of internal standards, D_{31}-160/181 PE and D_{31}-160/181 PS. Quantification was based on calibration curves constructed using PE and PS standards with multiple reactions monitoring function. PE calibration curves include 160 LPE, 181 LPE, 160/181 PE, 160,182 PE, 180,182 PE, 180/204 ES. PE and PS species without reference compounds were quantified with the standard sharing the closest structure. PS calibration curves include 160 LPS, 181 LPS, 180 LPS, 160/181 PS, 160,182 PS, 180,182 PS, 180/204 PS. Final concentration of PE and PS were normalized to DNA contents in the cell and expressed as ng/mg DNA.

NMR Metabolomics analysis

Sample processing: The hydrophilic cell extracts were dried in a SpeedVac centrifuge for 4–6 h at room temperature, and stored at 20°C until data collection. The dried polar extracts were re-hydrated with 600 μL of NMR buffer containing 100 mM phosphate buffer, pH 7.3,

1 mM TMSP (3-Trimethylsilyl 2,2,3,3-d4 propionate, CAS 24493–21-8), and 1 mg/mL NaN3 (sodium azide CAS 26627–22-8) prepared in D_2O.

Media samples were thawed on ice and centrifuged 4000 × g_n for 5 min at 4°C. The 500 μL supernatant of the media samples were aliquoted onto pre-washed 3 kDa spin filters (NANOSEP 3K, Pall Life Sciences), and centrifuged 10000 × g_n for 90 min at 4°C. The 300 mL of media filtrate was mixed with 300 μL of NMR buffer.

NMR data collection: One-dimensional ^{1}H NMR spectra were recorded on all samples using the nuclear overhauser spectroscopy (NOESY) pulse sequence with presaturation of the water peak on a Bruker Avance II 600 MHz spectrometer. Two-dimensional ^{13}C edited heteronuclear single quantum correlation (HSQC) spectra for representative samples were acquired to assess the metabolites annotation. All NMR data were processed using Topspin 3.1 software (Bruker Analytik, Rheinstetten, Germany). All FIDs were subjected to an exponential line-broadening of 0.3 Hz. Upon Fourier transformation, each spectrum was manually phased, baseline corrected, and referenced to the internal standard TMSP at 0.0 ppm. Metabolites found in cell extract and media were assigned based on 1D ^{1}H and 2D NMR experiments with reference spectra found in databases, such as the Human Metabolome Database and Chenomx ®NMR Suite profiling software (Chenomx Inc. version 8.1).

QUANTIFICATION AND STATISTICAL ANALYSIS

Western blot analyses were quantified using the Li-Cor imaging system software. All data, with the exception of NMR and targeted lipidomics, listed separately below, are presented as mean ± SD. Statistical analyzes utilized GraphPad Prism 7, and statistical significance was determined using one-way analysis of variance (ANOVA) with Turkey HSD (Honestly Significant Difference) calculation to compare multiple treatments.

NMR Metabolomics Data analysis

^{1}H NMR spectra were processed and analyzed with AMIX for PCA analysis and the spectral bucket intensity tables were generated for further analysis. The spectra from 0.5 to 10.0 ppm, excluding the region of the residual water resonance (4.6 to 5.0 ppm), methanol (3.36–3.38 ppm), and phenformin (3.49–3.54, 7.29–7.43ppm) were reduced by uniform binning to 1916 buckets 0.005 ppm wide. The spectra were normalized to constant total spectral area prior to PCA analysis and the binned spectra were mean-centered with no scaling.

The metabolites assigned bin-by-bin differences between each group were assessed by univariate approach. Pairwise differences within each bin were compared using a two-tailed Welch’s t test, the false discovery rate (FDR) was controlled at the 0.05 level using the Benjamini-Hochberg method (Benjamini and Hochberg, 1995).

DATA AND SOFTWARE AVAILABILITY

The NMR and lipidomics datasets reported in this paper are available at Mendeley Data: https://doi.org/10.17632/ccx58pdy3d.1.

Supplementary Material

Refer to Web version on PubMed Central for supplementary material.

ACKNOWLEDGMENTS

We would like to acknowledge the service and contributions of Drs. Wujuan Zhang and Kenneth Setchell at the Mass Spectrometry Core Facility and Drs. Miki Watanabe and Lindsey Romick-Rosendale in the NMR-based Metabolomics Core, both at Cincinnati Children's Hospital. We thank Drs. Atsuo Sasaki and Yoshiki Ikeda (UC Hem/Onc) for their assistance with HPLC measurement of nucleotides, Dr. Maria Czyzyk-krzeska and Megan Bischoff (UC Department of Cancer Biology) for sharing their protocol and expertise in LC3B immunofluorescence, and Dr. Birgit Ehmer (UC Department of Cancer Biology Microscopy Laboratory) for her knowledge and assistance with confocal microscopy. We also express our gratitude to Drs. Michael T. Ryan for sharing the NDUF KO cell lines, Heeseon An and Wade Harper for sharing the Keima mitophagy reporter cells, and Patrick Dennis for his critical reading of the manuscript. This work was supported by funding from the National Cancer Institute (R21CA191814) and the Hematology Oncology Translational Science and Pilot Grant Award (HOTSA/HOTGA) program at the University of Cincinnati.

REFERENCES

Amaravadi RK, Lippincott-Schwartz J, Yin XM, Weiss WA, Takebe N, Timmer W, DiPaola RS, Lotze MT, and White E (2011). Principles and current strategies for targeting autophagy for cancer treatment. Clin. Cancer Res 17, 654–666. [PubMed: 21325294]

An H, and Harper JW (2018). Systematic analysis of ribophagy in human cells reveals bystander flux during selective autophagy. Nat. Cell Biol 20, 135–143. [PubMed: 29230017]

Auciello FR, Ross FA, Ikematsu N, and Hardie DG (2014). Oxidative stress activates AMPK in cultured cells primarily by increasing cellular AMP and/or ADP. FEBS Lett. 588, 3361–3366. [PubMed: 25084564]

Benjamini Y, and Hochberg Y (1995). Controlling the False Discovery Rate: A Practical and Powerful Approach to Multiple Testing. J. R. Stat. Soc. B 57, 289–300.

Birsoy K, Wang T, Chen WW, Freinkman E, Abu-Remaileh M, and Sabatini DM (2015). An Essential Role of the Mitochondrial Electron Transport Chain in Cell Proliferation Is to Enable Aspartate Synthesis. Cell 162, 540–551. [PubMed: 26232224]

Bové J, Martínez-Vicente M, and Vila M (2011). Fighting neurodegeneration with rapamycin: mechanistic insights. Nat. Rev. Neurosci 12, 437–452. [PubMed: 21772323]

Bravo-Sagua R, López-Crisosto C, Parra V, Rodriguez-Peña M, Rothermel BA, Quest AF, and Lavandero S (2016). mTORC1 inhibitor rapamycin and ER stressor tunicamycin induce differential patterns of ER-mitochondria coupling. Sci. Rep 6, 36394. [PubMed: 27808250]

Buzzai M, Bauer DE, Jones RG, Deberardinis RJ, Hatzivassiliou G, Elstrom RL, and Thompson CB (2005). The glucose dependence of Akttransformed cells can be reversed by pharmacologic activation of fatty acid beta-oxidation. Oncogene 24, 4165–4173. [PubMed: 15806154]

Calzada E, Onguka O, and Claypool SM (2016). Phosphatidylethanolamine Metabolism in Health and Disease. Int. Rev. Cell Mol. Biol 321, 29–88. [PubMed: 26811286]

Chen CA, and Okayama H (1988). Calcium phosphate-mediated gene transfer: a highly efficient transfection system for stably transforming cells with plasmid DNA. Biotechniques 6, 632–638. [PubMed: 3273409]

Cheong H, Lindsten T, Wu J, Lu C, and Thompson CB (2011). Ammonia-induced autophagy is independent of ULK1/ULK2 kinases. Proc. Natl. Acad. Sci. USA 108, 11121–11126. [PubMed: 21690395]

Corominas-Faja B, Quirantes-Piné R, Oliveras-Ferraros C, Vazquez-Martin A, Cufí S, Martin-Castillo B, Micol V, Joven J, Segura-Carretero A, and Menendez JA (2012). Metabolomic fingerprint reveals that metformin impairs one-carbon metabolism in a manner similar to the antifolate class of chemotherapy drugs. Aging (Albany N.Y.) 4, 480–498.

Cunningham JT, Rodgers JT, Arlow DH, Vazquez F, Mootha VK, and Puigserver P (2007). mTOR controls mitochondrial oxidative function through a YY1-PGC-1alpha transcriptional complex. Nature 450, 736–740. [PubMed: 18046414]

DeBosch BJ, Heitmeier MR, Mayer AL, Higgins CB, Crowley JR, Kraft TE, Chi M, Newberry EP, Chen Z, Finck BN, et al. (2016). Trehalose inhibits solute carrier 2A (SLC2A) proteins to induce autophagy and prevent hepatic steatosis. Sci. Signal 9, ra21. [PubMed: 26905426]

Dennis PB, and Mercer CA (2009). The GST-BHMT assay and related assays for autophagy. Methods Enzymol. 452, 97–118. [PubMed: 19200878]

Di Bartolomeo F, Wagner A, and Daum G (2017). Cell biology, physiology and enzymology of phosphatidylserine decarboxylase. Biochim. Biophys. Acta 1862, 25–38.

Diwu Z, Chen CS, Zhang C, Klaubert DH, and Haugland RP (1999). A novel acidotropic pH indicator and its potential application in labeling acidic organelles of live cells. Chem. Biol 6, 411–418. [PubMed: 10381401]

Egan DF, Shackelford DB, Mihaylova MM, Gelino S, Kohnz RA, Mair W, Vasquez DS, Joshi A, Gwinn DM, Taylor R, et al. (2011). Phosphorylation of ULK1 (hATG1) by AMP-activated protein kinase connects energy sensing to mitophagy. Science 331, 456–461. [PubMed: 21205641]

Farré JC, and Subramani S (2016). Mechanistic insights into selective autophagy pathways: lessons from yeast. Nat. Rev. Mol. Cell Biol 17, 537–552. [PubMed: 27381245]

Gomes LC, Di Benedetto G, and Scorrano L (2011). During autophagy mitochondria elongate, are spared from degradation and sustain cell viability. Nat. Cell Biol 13, 589–598. [PubMed: 21478857]

Graef M, and Nunnari J (2011). Mitochondria regulate autophagy by conserved signalling pathways. EMBO J. 30, 2101–2114. [PubMed: 21468027]

Guo JY, Teng X, Laddha SV, Ma S, Van Nostrand SC, Yang Y, Khor S, Chan CS, Rabinowitz JD, and White E (2016). Autophagy provides metabolic substrates to maintain energy charge and nucleotide pools in Ras-driven lung cancer cells. Genes Dev. 30, 1704–1717. [PubMed: 27516533]

Gwinn DM, Shackelford DB, Egan DF, Mihaylova MM, Mery A, Vasquez DS, Turk BE, and Shaw RJ (2008). AMPK phosphorylation of raptor mediates a metabolic checkpoint. Mol. Cell 30, 214–226. [PubMed: 18439900]

Hailey DW, Rambold AS, Satpute-Krishnan P, Mitra K, Sougrat R, Kim PK, and Lippincott-Schwartz J (2010). Mitochondria supply membranes for autophagosome biogenesis during starvation. Cell 141, 656–667. [PubMed: 20478256]

Hamasaki M, Furuta N, Matsuda A, Nezu A, Yamamoto A, Fujita N, Oomori H, Noda T, Haraguchi T, Hiraoka Y, et al. (2013). Autophagosomes form at ER-mitochondria contact sites. Nature 495, 389–393. [PubMed: 23455425]

Hara T, Nakamura K, Matsui M, Yamamoto A, Nakahara Y, Suzuki-Migishima R, Yokoyama M, Mishima K, Saito I, Okano H, and Mizushima N (2006). Suppression of basal autophagy in neural cells causes neurodegenerative disease in mice. Nature 441, 885–889. [PubMed: 16625204]

Ichimura Y, Kirisako T, Takao T, Satomi Y, Shimonishi Y, Ishihara N, Mizushima N, Tanida I, Kominami E, Ohsumi M, et al. (2000). A ubiquitin-like system mediates protein lipidation. Nature 408, 488–492. [PubMed: 11100732]

Inoki K, Zhu T, and Guan KL (2003). TSC2 mediates cellular energy response to control cell growth and survival. Cell 115, 577–590. [PubMed: 14651849]

Jang SY, Kang HT, and Hwang ES (2012). Nicotinamide-induced mitophagy: event mediated by high NAD+/NADH ratio and SIRT1 protein activation. J. Biol. Chem 287, 19304–19314. [PubMed: 22493485]

Johnson SC, Yanos ME, Kayser EB, Quintana A, Sangesland M, Castanza A, Uhde L, Hui J, Wall VZ, Gagnidze A, et al. (2013). mTOR inhibition alleviates mitochondrial disease in a mouse model of Leigh syndrome. Science 342, 1524–1528. [PubMed: 24231806]

Kabeya Y, Mizushima N, Ueno T, Yamamoto A, Kirisako T, Noda T, Kominami E, Ohsumi Y, and Yoshimori T (2000). LC3, a mammalian homologue of yeast Apg8p, is localized in autophagosome membranes after processing. EMBO J. 19, 5720–5728. [PubMed: 11060023]

Kabeya Y, Mizushima N, Yamamoto A, Oshitani-Okamoto S, Ohsumi Y, and Yoshimori T (2004). LC3, GABARAP and GATE16 localize to autophagosomal membrane depending on form-II formation. J. Cell Sci 117, 2805–2812. [PubMed: 15169837]

Kalender A, Selvaraj A, Kim SY, Gulati P, Bru^lé S, Viollet B, Kemp BE, Bardeesy N, Dennis P, Schlager JJ, et al. (2010). Metformin, independent of AMPK, inhibits mTORC1 in a rag GTPase-dependent manner. Cell Metab. 11, 390–401. [PubMed: 20444419]

Katayama H, Kogure T, Mizushima N, Yoshimori T, and Miyawaki A (2011). A sensitive and quantitative technique for detecting autophagic events based on lysosomal delivery. Chem. Biol 18, 1042–1052. [PubMed: 21867919]

Kaur J, and Debnath J (2015). Autophagy at the crossroads of catabolism and anabolism. Nat. Rev. Mol. Cell Biol 16, 461–472. [PubMed: 26177004]

Kim J, Kundu M, Viollet B, and Guan KL (2011). AMPK and mTOR regulate autophagy through direct phosphorylation of Ulk1. Nat. Cell Biol 13, 132–141. [PubMed: 21258367]

Kimmelman AC, and White E (2017). Autophagy and Tumor Metabolism. Cell Metab. 25, 1037–1043. [PubMed: 28467923]

Li S, Li X, Guo H, Liu S, Huang H, Liu N, Yang C, Tang P, and Liu J (2013). Intracellular ATP concentration contributes to the cytotoxic and cytoprotective effects of adenosine. PLoS ONE 8, e76731. [PubMed: 24098558]

Li TY, Sun Y, Liang Y, Liu Q, Shi Y, Zhang CS, Zhang C, Song L, Zhang P, Zhang X, et al. (2016). ULK1/2 Constitute a Bifurcate Node Controlling Glucose Metabolic Fluxes in Addition to Autophagy. Mol. Cell 62, 359–370. [PubMed: 27153534]

Locasale JW (2013). Serine, glycine and one-carbon units: cancer metabolism in full circle. Nat. Rev. Cancer 13, 572–583. [PubMed: 23822983]

Lockwood TD (2010). The lysosome among targets of metformin: new antiinflammatory uses for an old drug? Expert Opin. Ther. Targets 14, 467–478. [PubMed: 20392164]

Lorin S, Hamaï A, Mehrpour M, and Codogno P (2013). Autophagy regulation and its role in cancer. Semin. Cancer Biol 23, 361–379. [PubMed: 23811268]

Madiraju AK, Erion DM, Rahimi Y, Zhang XM, Braddock DT, Albright RA, Prigaro BJ, Wood JL, Bhanot S, MacDonald MJ, et al. (2014). Metformin suppresses gluconeogenesis by inhibiting mitochondrial glycerophosphate dehydrogenase. Nature 510, 542–546. [PubMed: 24847880]

Marroquin LD, Hynes J, Dykens JA, Jamieson JD, and Will Y (2007). Circumventing the Crabtree effect: replacing media glucose with galactose increases susceptibility of HepG2 cells to mitochondrial toxicants. Toxicol. Sci 97, 539–547. [PubMed: 17361016]

Meijer AJ, and Codogno P (2011). Autophagy: regulation by energy sensing. Curr. Biol 21, R227–R229. [PubMed: 21419990]

Meley D, Bauvy C, Houben-Weerts JH, Dubbelhuis PF, Helmond MT, Codogno P, and Meijer AJ (2006). AMP-activated protein kinase and the regulation of autophagic proteolysis. J. Biol. Chem 281, 34870–34879. [PubMed: 16990266]

Melser S, Chatelain EH, Lavie J, Mahfouf W, Jose C, Obre E, Goorden S, Priault M, Elgersma Y, Rezvani HR, et al. (2013). Rheb regulates mitophagy induced by mitochondrial energetic status. Cell Metab. 17, 719–730. [PubMed: 23602449]

Menzies FM, Fleming A, Caricasole A, Bento CF, Andrews SP, Ashkenazi A, Füllgrabe J, Jackson A, Jimenez Sanchez M, Karabiyik C, et al. (2017). Autophagy and Neurodegeneration: Pathogenic Mechanisms and Therapeutic Opportunities. Neuron 93, 1015–1034. [PubMed: 28279350]

Mercer CA, Kaliappan A, and Dennis PB (2008). Macroautophagy-dependent, intralysosomal cleavage of a betaine homocysteine methyltransferase fusion protein requires stable multimerization. Autophagy 4, 185–194. [PubMed: 18059170]

Mercer CA, Kaliappan A, and Dennis PB (2009). A novel, human Atg13 binding protein, Atg101, interacts with ULK1 and is essential for macroautophagy. Autophagy 5, 649–662. [PubMed: 19287211]

Miyata N, Watanabe Y, Tamura Y, Endo T, and Kuge O (2016). Phosphatidylserine transport by Ups2-Mdm35 in respiration-active mitochondria. J. Cell Biol 214, 77–88. [PubMed: 27354379]

Morita M, Gravel SP, Chénard V, Sikström K, Zheng L, Alain T, Gandin V, Avizonis D, Arguello M, Zakaria C, et al. (2013). mTORC1 controls mitochondrial activity and biogenesis through 4E-BP-dependent translational regulation. Cell Metab. 18, 698–711. [PubMed: 24206664]

Naon D, and Scorrano L (2014). At the right distance: ER-mitochondria juxtaposition in cell life and death. Biochim. Biophys. Acta 1843, 2184–2194. [PubMed: 24875902]

Narendra DP, Jin SM, Tanaka A, Suen DF, Gautier CA, Shen J, Cookson MR, and Youle RJ (2010). PINK1 is selectively stabilized on impaired mitochondria to activate Parkin. PLoS Biol. 8, e1000298. [PubMed: 20126261]

Noda T (2017). Regulation of Autophagy through TORC1 and mTORC1. Biomolecules 7, E52. [PubMed: 28686223]

Owen MR, Doran E, and Halestrap AP (2000). Evidence that metformin exerts its anti-diabetic effects through inhibition of complex 1 of the mitochondrial respiratory chain. Biochem. J 348, 607–614. [PubMed: 10839993]

Palmer G, Horgan DJ, Tisdale H, Singer TP, and Beinert H (1968). Studies on the respiratory chain-linked reduced nicotinamide adenine dinucleotide dehydrogenase. XIV. Location of the sites of inhibition of rotenone, barbiturates, and piericidin by means of electron paramagnetic resonance spectroscopy. J. Biol. Chem 243, 844–847. [PubMed: 4295607]

Pankiv S, Clausen TH, Lamark T, Brech A, Bruun JA, Outzen H, Øver-vatn A, Bjørkøy G, and Johansen T (2007). p62/SQSTM1 binds directly to Atg8/LC3 to facilitate degradation of ubiquitinated protein aggregates by autophagy. J. Biol. Chem 282, 24131–24145. [PubMed: 17580304]

Pickles S, Vigié P, and Youle RJ (2018). Mitophagy and Quality Control Mechanisms in Mitochondrial Maintenance. Curr. Biol 28, R170–R185. [PubMed: 29462587]

Pickrell AM, and Youle RJ (2015). The roles of PINK1, parkin, and mitochondrial fidelity in Parkinson's disease. Neuron 85, 257–273. [PubMed: 25611507]

Pietrocola F, Izzo V, Niso-Santano M, Vacchelli E, Galluzzi L, Maiuri MC, and Kroemer G (2013). Regulation of autophagy by stress-responsive transcription factors. Semin. Cancer Biol 23, 310–322. [PubMed: 23726895]

Plomp PJ, Gordon PB, Meijer AJ, Høyvik H, and Seglen PO (1989). Energy dependence of different steps in the autophagic-lysosomal pathway. J. Biol. Chem 264, 6699–6704. [PubMed: 2708336]

Polson HE, de Lartigue J, Rigden DJ, Reedijk M, Urbé S, Clague MJ, and Tooze SA (2010). Mammalian Atg18 (WIPI2) localizes to omegasomeanchored phagophores and positively regulates LC3 lipidation. Autophagy 6, 506–522. [PubMed: 20505359]

Prabhu V, Srivastava P, Yadav N, Amadori M, Schneider A, Seshadri A, Pitarresi J, Scott R, Zhang H, Koochekpour S, et al. (2013). Resveratrol depletes mitochondrial DNA and inhibition of autophagy enhances resveratrol-induced caspase activation. Mitochondrion 13, 493–499. [PubMed: 23088850]

Ramirez-Peinado S, Leon-Annicchiarico CL, Galindo-Moreno J, Iurlaro R, Caro-Maldonado A, Prehn JH, Ryan KM, and Munoz-Pinedo C (2013). Glucose-starved cells do not engage in prosurvival autophagy. J. Biol. Chem 288, 30387–30398. [PubMed: 24014036]

Rockenfeller P, Koska M, Pietrocola F, Minois N, Knittelfelder O, Sica V, Franz J, Carmona-Gutierrez D, Kroemer G, and Madeo F (2015). Phosphatidylethanolamine positively regulates autophagy and longevity. Cell Death Differ. 22, 499–508. [PubMed: 25571976]

Rodenburg RJ (2016). Mitochondrial complex I-linked disease. Biochim. Biophys. Acta 1857, 938–945. [PubMed: 26906428]

Roser M, Josic D, Kontou M, Mosetter K, Maurer P, and Reutter W (2009). Metabolism of galactose in the brain and liver of rats and its conversion into glutamate and other amino acids. J. Neural Transm. (Vienna) 116, 131–139. [PubMed: 19089315]

Russell RC, Yuan HX, and Guan KL (2014). Autophagy regulation by nutrient signaling. Cell Res. 24, 42–57. [PubMed: 24343578]

Samari HR, and Seglen PO (1998). Inhibition of hepatocytic autophagy by adenosine, aminoimidazole-4-carboxamide riboside, and N6-mercaptopurine riboside. Evidence for involvement of amp-activated protein kinase. J. Biol. Chem 273, 23758–23763. [PubMed: 9726984]

Sancak Y, Bar-Peled L, Zoncu R, Markhard AL, Nada S, and Sabatini DM (2010). Ragulator-Rag complex targets mTORC1 to the lysosomal surface and is necessary for its activation by amino acids. Cell 141, 290–303. [PubMed: 20381137]

Sarkar S, Davies JE, Huang Z, Tunnacliffe A, and Rubinsztein DC (2007). Trehalose, a novel mTOR-independent autophagy enhancer, accelerates the clearance of mutant huntingtin and alpha-synuclein. J. Biol. Chem 282, 5641–5652. [PubMed: 17182613]

Schellens JP, and Meijer AJ (1991). Energy depletion and autophagy. Cytochemical and biochemical studies in isolated rat hepatocytes. Histochem. J 23, 460–466. [PubMed: 1743994]

Shackelford DB, Abt E, Gerken L, Vasquez DS, Seki A, Leblanc M, Wei L, Fishbein MC, Czernin J, Mischel PS, and Shaw RJ (2013). LKB1 inactivation dictates therapeutic response of non-small cell lung cancer to the metabolism drug phenformin. Cancer Cell 23, 143–158. [PubMed: 23352126]

Shiao YJ, Lupo G, and Vance JE (1995). Evidence that phosphatidylserine is imported into mitochondria via a mitochondria-associated membrane and that the majority of mitochondrial phosphatidylethanolamine is derived from decarboxylation of phosphatidylserine. J. Biol. Chem 270, 11190–11198. [PubMed: 7744750]

Shin HJ, Kim H, Oh S, Lee JG, Kee M, Ko HJ, Kweon MN, Won KJ, and Baek SH (2016). AMPK-SKP2-CARM1 signalling cascade in transcriptional regulation of autophagy. Nature 534, 553–557. [PubMed: 27309807]

Stroud DA, Surgenor EE, Formosa LE, Reljic B, Frazier AE, Dibley MG, Osellame LD, Stait T, Beilharz TH, Thorburn DR, et al. (2016). Accessory subunits are integral for assembly and function of human mitochondrial complex I. Nature 538, 123–126. [PubMed: 27626371]

Sullivan LB, Gui DY, Hosios AM, Bush LN, Freinkman E, and Vander Heiden MG (2015). Supporting Aspartate Biosynthesis Is an Essential Function of Respiration in Proliferating Cells. Cell 162, 552–563. [PubMed: 26232225]

Theurey P, Tubbs E, Vial G, Jacquemetton J, Bendridi N, Chauvin MA, Alam MR, Le Romancer M, Vidal H, and Rieusset J (2016). Mitochondriaassociated endoplasmic reticulum membranes allow adaptation of mitochondrial metabolism to glucose availability in the liver. J. Mol. Cell Biol 8, 129–143. [PubMed: 26892023]

Thomas HE, Mercer CA, Carnevalli LS, Park J, Andersen JB, Conner EA, Tanaka K, Matsutani T, Iwanami A, Aronow BJ, et al. (2012). mTOR inhibitors synergize on regression, reversal of gene expression, and autophagy in hepatocellular carcinoma. Sci. Transl. Med 4, 139ra84.

Toyama EQ, Herzig S, Courchet J, Lewis TL, Jr., Losón OC, Hellberg K, Young NP, Chen H, Polleux F, Chan DC, and Shaw RJ (2016). Metabolism. AMP-activated protein kinase mediates mitochondrial fission in response to energy stress. Science 351, 275–281. [PubMed: 26816379]

Tubbs E, and Rieusset J (2016). Study of Endoplasmic Reticulum and Mitochondria Interactions by In Situ Proximity Ligation Assay in Fixed Cells. J. Vis. Exp, 118, e54899.

Vance JE, and Tasseva G (2013). Formation and function of phosphatidylserine and phosphatidylethanolamine in mammalian cells. Biochim. Biophys. Acta 1831, 543–554. [PubMed: 22960354]

Veiga SR, Ge X, Mercer CA, Herná ndez-Á lvarez MI, Thomas HE, Hernandez-Losa J, Ramó n Y Cajal S, Zorzano A, Thomas G, and Kozma SC(2018). Phenformin-Induced Mitochondrial Dysfunction Sensitizes Hepatocellular Carcinoma for Dual Inhibition of mTOR. Clin. Cancer Res. 24, 3767–3780. [PubMed: 29691292]

Venegas V, and Halberg MC (2012). Measurement of mitochondrial DNA copy number. Methods Mol. Biol. 837, 327–335. [PubMed: 22215558]

Voelker DR (1993). The ATP-dependent translocation of phosphatidylserine to the mitochondria is a process that is restricted to the autologous organelle. J. Biol. Chem 268, 7069–7074. [PubMed: 8463240]

Wang Z, Wilson WA, Fujino MA, and Roach PJ (2001). Antagonistic controls of autophagy and glycogen accumulation by Snf1p, the yeast homolog of AMP-activated protein kinase, and the cyclin-dependent kinase Pho85p. Mol. Cell. Biol 21, 5742–5752. [PubMed: 11486014]

Weinberg SE, and Chandel NS (2015). Targeting mitochondria metabolism for cancer therapy. Nat. Chem. Biol 11, 9–15. [PubMed: 25517383]

Wieckowski MR, Giorgi C, Lebiedzinska M, Duszynski J, and Pinton P (2009). Isolation of mitochondria-associated membranes and mitochondria from animal tissues and cells. Nat. Protoc 4, 1582–1590. [PubMed: 19816421]

Wilson-Zbinden C, dos Santos AX, Stoffel-Studer I, van der Vaart A, Hofmann K, Reggiori F, Riezman H, Kraft C, and Peter M (2015). Autophagy competes for a common phosphatidylethanolamine pool with major cellular PE-consuming pathways in Saccharomyces cerevisiae. Genetics 199, 475–485. [PubMed: 25519895]

Wise DR, and Thompson CB (2010). Glutamine addiction: a new therapeutic target in cancer. Trends Biochem. Sci 35, 427–433. [PubMed: 20570523]

Yang Z, and Klionsky DJ (2010). Mammalian autophagy: core molecular machinery and signaling regulation. Curr. Opin. Cell Biol 22, 124–131. [PubMed: 20034776]

Yang S, Wang X, Contino G, Liesa M, Sahin E, Ying H, Bause A, Li Y, Stommel JM, Dell'antonio G, et al. (2011). Pancreatic cancers require autophagy for tumor growth. Genes Dev. 25, 717–729. [PubMed: 21406549]

Yoshii SR, Kishi C, Ishihara N, and Mizushima N (2011). Parkin mediates proteasome-dependent protein degradation and rupture of the outer mitochondrial membrane. J. Biol. Chem 286, 19630–19640. [PubMed: 21454557]

Youle RJ, and Narendra DP (2011). Mechanisms of mitophagy. Nat. Rev. Mol. Cell Biol 12, 9–14. [PubMed: 21179058]

Zhang S, Zeng X, Ren M, Mao X, and Qiao S (2017). Novel metabolic and physiological functions of branched chain amino acids: a review. J. Anim. Sci. Biotechnol 8, 10. [PubMed: 28127425]

Zheng X, Boyer L, Jin M, Kim Y, Fan W, Bardy C, Berggren T, Evans RM, Gage FH, and Hunter T (2016). Alleviation of neuronal energy deficiency by mTOR inhibition as a treatment for mitochondria-related neurodegeneration. eLife 5, e13378. [PubMed: 27008180]

Zoncu R, Bar-Peled L, Efeyan A, Wang S, Sancak Y, and Sabatini DM (2011). mTORC1 senses lysosomal amino acids through an inside-out mechanism that requires the vacuolar H(+)-ATPase. Science 334, 678–683. [PubMed: 22053050]

Highlights

- Phenformin, metformin, and mitochondrial complex I defects suppress autophagy
- Defects in glycolysis and OXPHOS have opposing effects on autophagy
- Autophagy is enhanced by a metabolic shift toward OXPHOS
- Mitochondrial-associated membranes and mitochondrial PE support autophagy

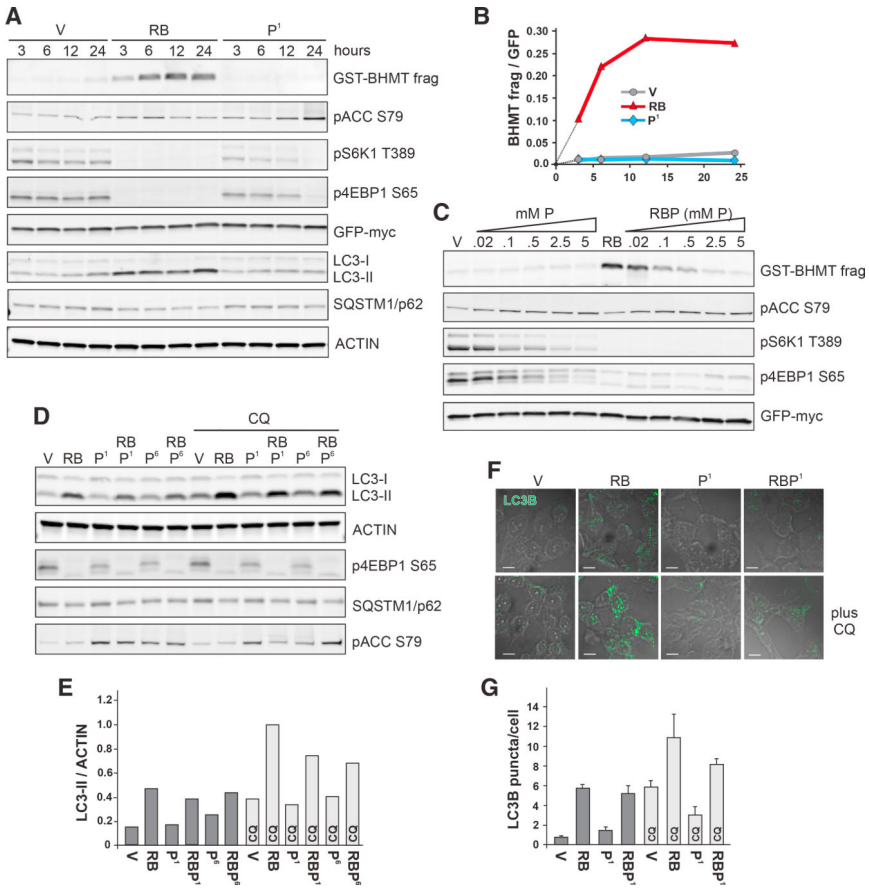

Figure 1. Phenformin Inhibits Autophagy Induced by mTOR Inhibitors

(A and B) Time course of GST-BHMT autophagy assay (A) and plotted ratio of the BHMT fragment/ GFP-myc (B) in HEK293 cells treated with vehicle (V), 5 nM RAD001 and 20 nM BEZ235 (RB), or 1 mM phenformin (P^1).

(C) GST-BHMT assay in HEK293 cells treated for 6 hr with 0–5 mM phenformin alone, or in combination with RB.

(D and E) LC3-II flux assay (D) and ratio of LC3-II/ACTIN (E) in HEK293 cells treated as indicated.

(F and G) Representative confocal images (F) and quantitation of LC3-B puncta/cell (G) in HEK293T cells. Treatments as in (D) and (E). Scale bar is 10 μm. Data represented as mean ± 1 SD.

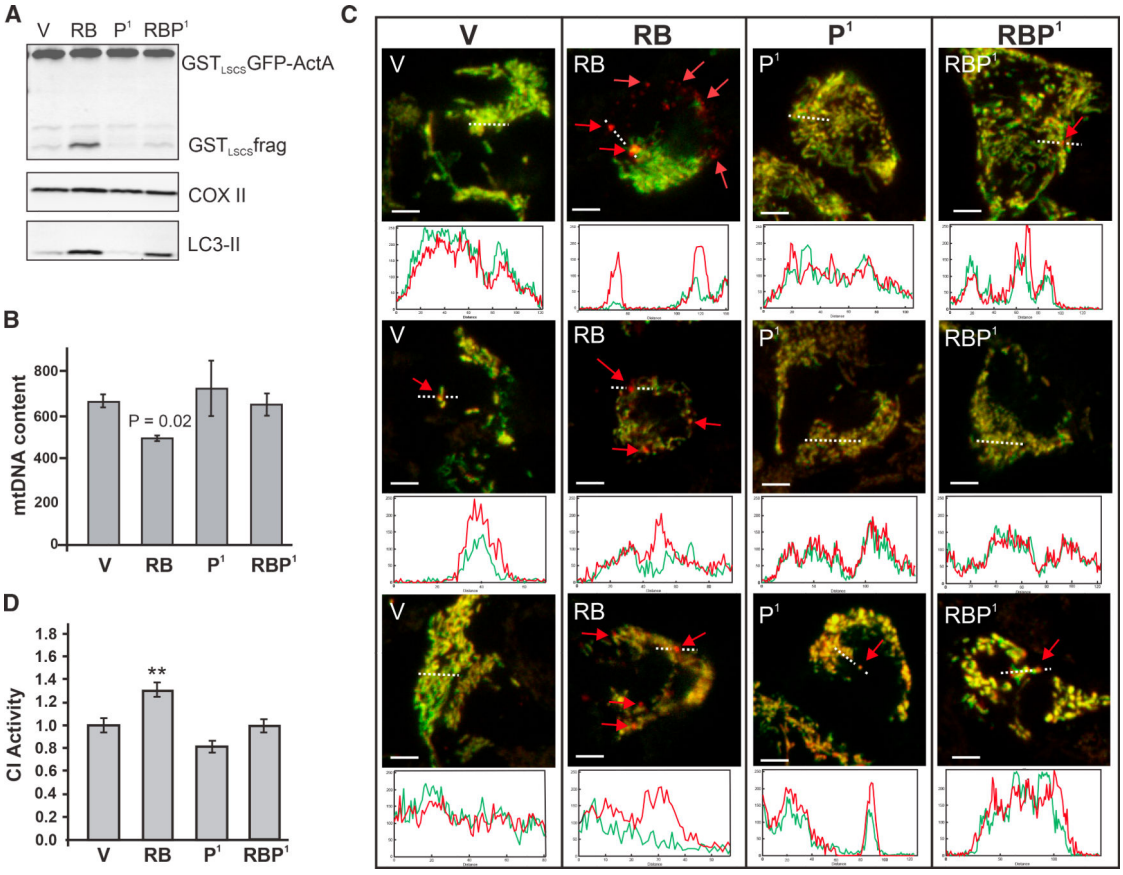

Figure 2. Phenformin Inhibits Mitophagy Induced by mTOR Inhibitors

(A) GST_{LSCS}GFP-ActA mitophagy assay in cells treated for 24 hr with V, RB, P^1, or RBP^1.

(B) Mitochondrial DNA content, as measured by RT-qPCR. Statistics by one-way ANOVA.

(C) Representative confocal images from Mito-Keima expressing cells, treated for 4 hr.

(D) Complex I activity in mitochondria purified from HEK293 cells. 16 hr treatments.

**Adjusted p value = 0.0074. Data represented as mean ± 1 SD.

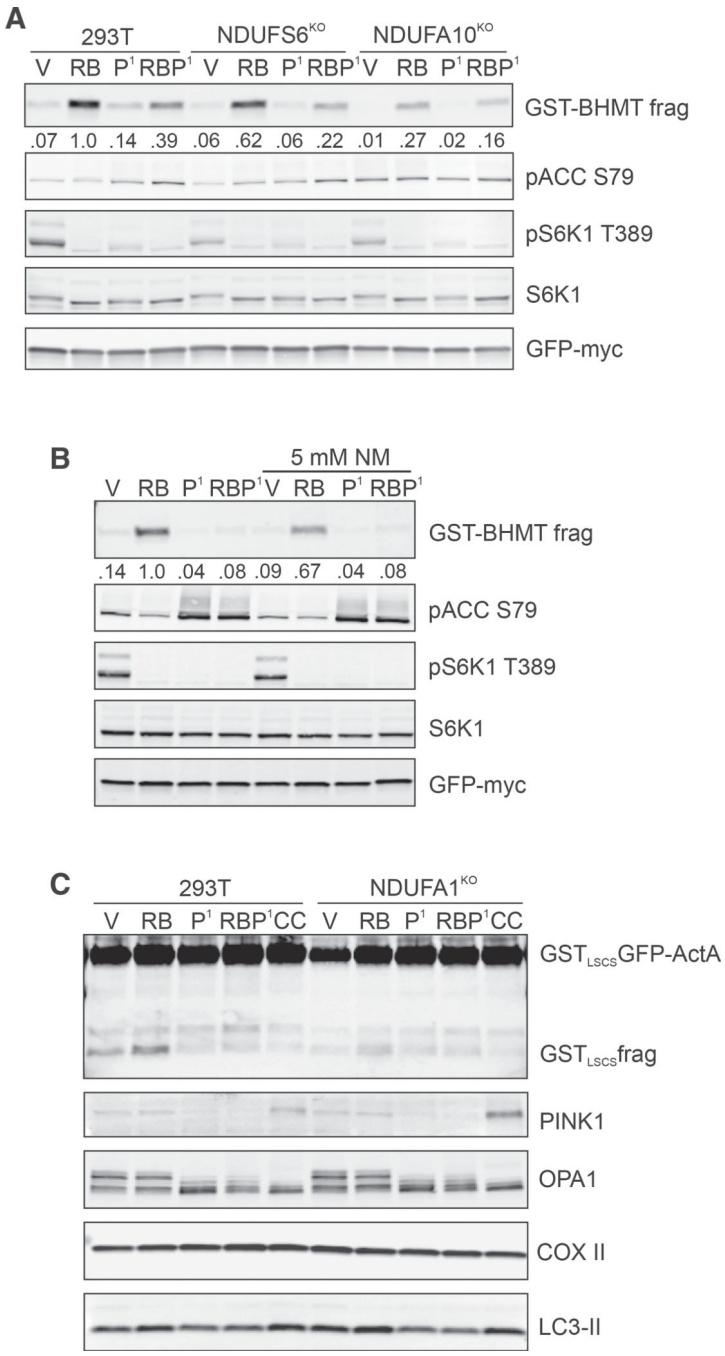

Figure 3. Autophagy Is Inhibited by Severe Defects in Mitochondrial Complex I Accessory Subunits

(A) GST-BHMT assay in control and *NDUFS6* or *NDUFA10* knockout (KO) cells. 6 hr treatments. A numerical value for the BHMT fragment (frag)/GFP ratio, normalized to RB, is shown.

(B) GST-BHMT assay in HEK293 cells treated for 6 hr, with or without 5 mM nicotinamide (NM).

(C) GST_{LSCS}GFP-ActA mitophagy assay in HEK293T control and *NDUFA1*^{KO} cells treated for 20 hr with V, RB, P^1, RBP^1, or 10 μM CCCP (CC).

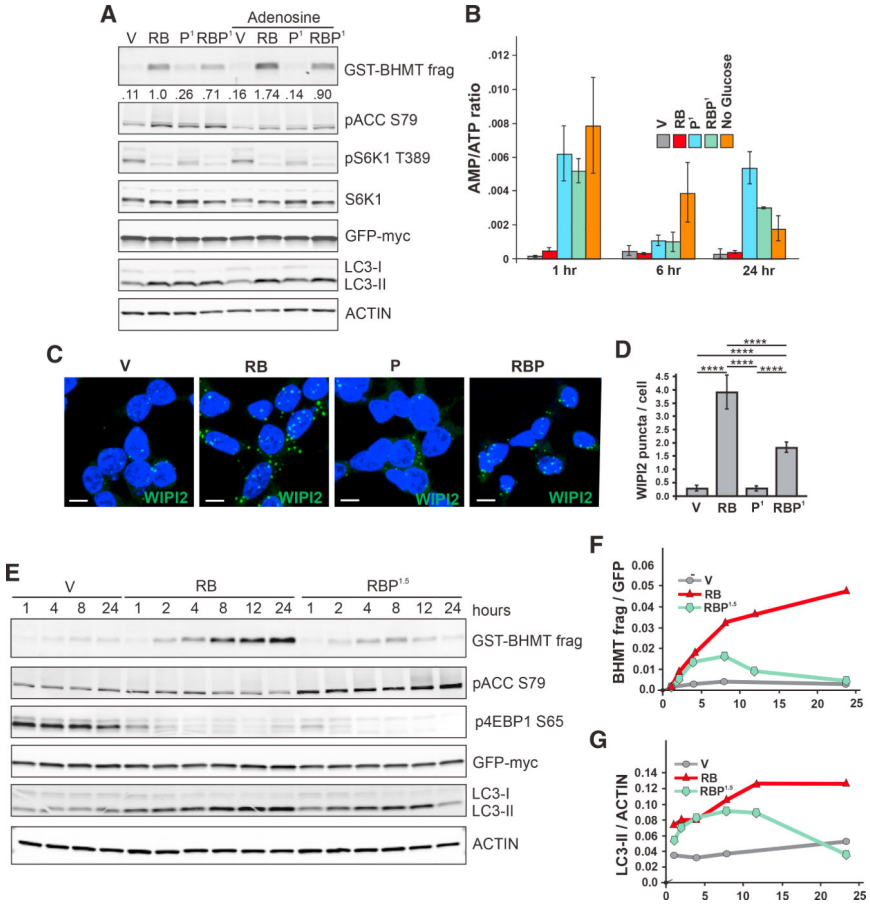

Figure 4. Phenformin Suppresses the Initiation, Amplitude, and Duration of Autophagy

(A) GST-BHMT assay in cells treated for 6 hr with V, RB, P^1, RBP^1, with or without 1 mM adenosine.

(B) Bar graph of AMP/ATP ratios in HEK293 cells treated with V, RB, P^1, RBP^1, or starved of glucose.

(C and D) Immunofluorescence of WIPI2 in HEK293T cells treated for 2 hr. Representative confocal images (C) and quantification of WIPI2 puncta (D). Scale bar is 10 μm.

(E–G) GST-BHMT time course assay in cells treated with V, RB, or $RBP^{1.5}$, as shown by western blotting (E) and graphs of BHMT frag/GFP ratios (F) and LC3-II/ACTIN ratios (G).

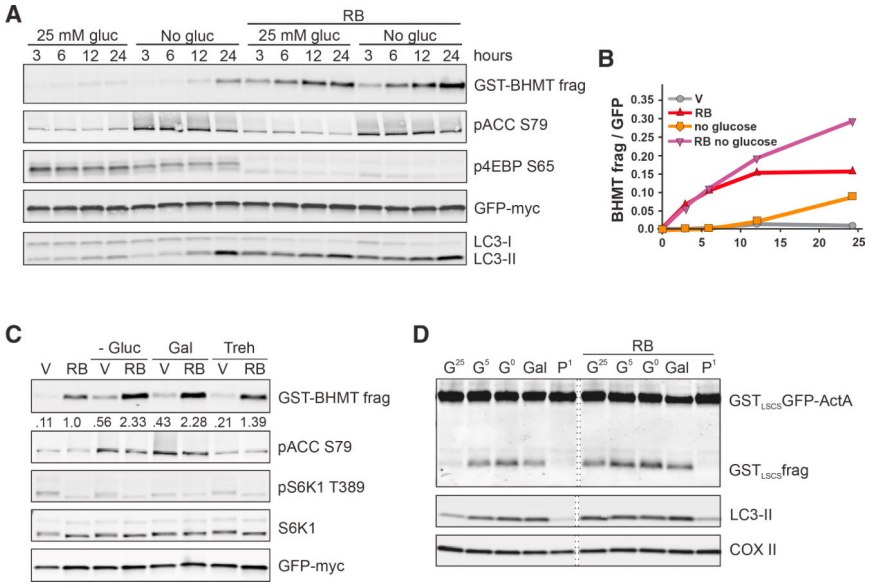

Figure 5. Glucose Starvation Increases Autophagy and Mitophagy

(A and B) GST-BHMT assay time course in cells treated with V or RB, in media with 25 or 0 mM glucose, as shown by western blotting (A) and graph of BHMT frag/GFP ratio (B).

(C) GST-BHMT assay in cells treated for 24 hr with vehicle or RB in DMEM with 25 or 0 mM glucose, 25 mM galactose (Gal), or 100 mM trehalose (Treh).

(D) GST_{LSCS}GFP-ActA mitophagy assay in cells treated for 24 hr with 25, 5, or 0 mM glucose; 25 mM Gal; or P^1, without or with RB.

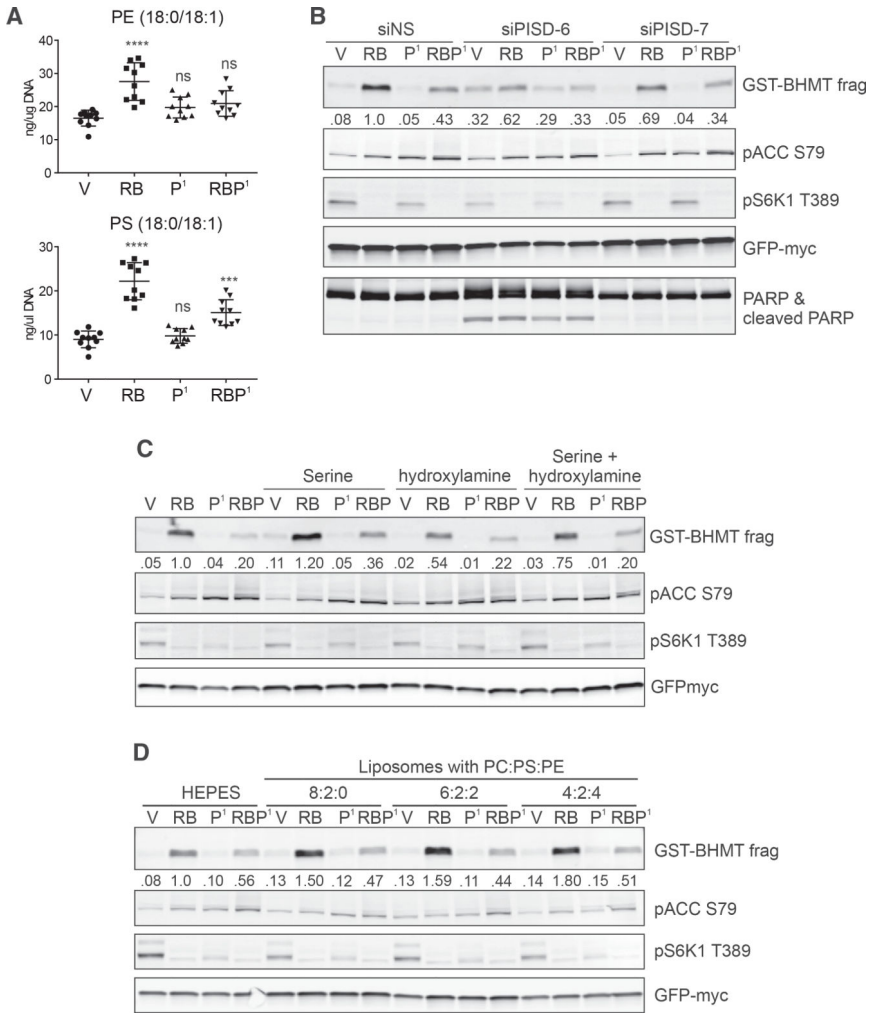

Figure 6. Phospholipid Remodeling in Autophagy

(A) Levels of PE (18:0/18:1) and PS (18:0/18:1) in HEK293 cells treated for 24 hr with V, RB, P^1, or RBP^1. ****p < 0.0001, ***p = 0.0002. ns = not significant. Data represented as mean ± 1 SD.

(B) GST-BHMT autophagy assay in cells transfected with non-silencing siRNA (siNS), siPISD-6, or siPISD-7. Cells were treated for 6 hr.

(C) GST-BHMT autophagy assay in cells treated for 6 hr with drugs as indicated, with 5 mM L-serine and/or 1 mM hydroxylamine as noted.

(D) GST-BHMT autophagy assay in cells treated for 6 hr as indicated, with buffer or mixed composition liposomes.

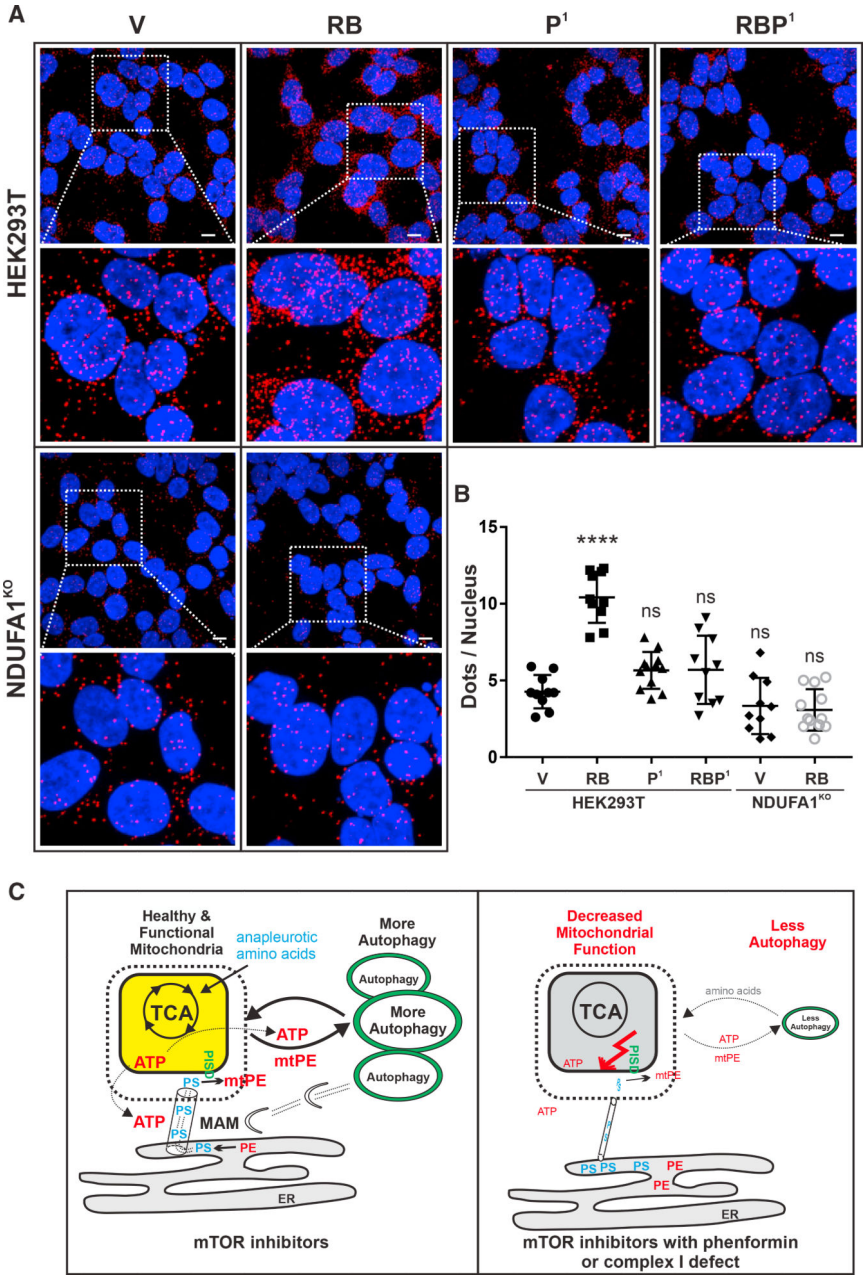

Figure 7. Defects in Complex I Prevent the Significant Increase in MAMs that Occurs with mTOR Inhibitors

(A) Proximity ligation assay showing MAMs by confocal microscopy. HEK293T cells were treated for 4 hr. Scale bar is 10 μm.

(B) Scatter plot graph showing quantified MAMs data. ****$p < 0.0001$. ns = not significant. Data represented as mean ± 1 SD.

(C) Model of conditions that support or inhibit autophagy. Left: mTOR inhibitors (RB) induce active autophagy in cells with healthy mitochondria by increasing MAMs, sites of ATG14 recruitment and phospholipid transport, supporting mtPE biosynthesis and sustained autophagy. RB autophagy is enhanced by conditions that increase TCA intermediates, ATP, or phospholipids. Right: Autophagy is impaired by phenformin or defects in complex I,

which prevent the increase of MAMs induced by mTOR inhibitors, local ATP, and the ATP-dependent transfer of PS for mtPE biosynthesis.